Simulation of the current and future dynamics of permafrost near the northern limit of permafrost on the Qinghai–Tibet Plateau

Jianting Zhao[1], Lin Zhao[1,2,3], Zhe Sun[1,~~34~~], Fujun Niu[5], Guojie ~~Hu~~[~~2~~]Hu[3], Defu ~~Zou~~[~~2~~]Zou[3], Guangyue ~~Liu~~[~~2~~]Liu[3], Erji ~~Du~~[~~2~~]Du[3], Chong Wang[1], Lingxiao Wang[1], Yongping ~~Qiao~~[~~2~~]Qiao[3], Jianzong ~~Shi~~[~~2~~]Shi[3], Yuxin Zhang[1], Junqiang Gao[6], Yuanwei Wang[1], Yan Li[1], Wenjun Yu[7], Huayun Zhou[2,~~43~~], Zanpin Xing[2,~~43~~], Minxuan Xiao[1], Luhui Yin[1], Shengfeng Wang[1]

[1] School of Geographical Sciences, Nanjing University of Information Science &Technology, Nanjing 210044, China

[2] University of Chinese Academy of Sciences, Beijing 101408, China

[3] Cryosphere Research Station on Qinghai–Xizang Plateau, State Key Laboratory of Cryospheric Sciences, Northwest Institute of Eco–Environment and Resources, Chinese Academy of Sciences, Lanzhou 730000, China

[~~3,4~~] Key Laboratory of Environment Change and Resources Use in Beibu Gulf, Ministry of Education, Nanning Normal University, Nanning 530001, China

[~~4~~] ~~University of Chinese Academy of Sciences, Beijing 101408, China~~

[5] State Key Laboratory of Frozen Soil Engineering, Northwest Institute of Eco–Environment and Resources, Chinese Academy of Sciences, Lanzhou 730000, China

[6] School of Mathematics and Statistics, Nanjing University of Information Science & Technology, Nanjing 210044, China

[7] School of Hydrology and Water Resources, Nanjing University of Information Science & Technology, Nanjing 210044, China

Correspondence to: Lin Zhao (lzhao@nuist.edu.cn)

Abstract: Permafrost has been warming and thawing ~~at a global scale~~ with subsequent effects on the climate, hydrological, and ecosystem ~~and engineering system~~. However, the ~~variation of permafrost thermal state~~ permafrost thermal state ~~in~~variation in the northern lower limit of the permafrost zone (Xidatan) on the Qinghai–~~Tibetan~~Tibet Plateau (QTP) is unclear. ~~To evaluate and project the permafrost changes, t~~This study attempt to explore the changes and variability of this permafrost using ~~simulated the spatiotemporal dynamics of this marginal permafrost~~ historical~~ly~~ (1970–2019) and future projections from Global Climate Model (GCM) outputs of Coupled Model Intercomparison Project Phase 5 and 6 (CMIP5, CMIP6)~~based on the detailed investigation and monitoring datasets from 1987 in this study region, improved remote sensing–based Land Surface Temperature product (LST) and climate projections from Global Climate Model (GCM) outputs of~~

~~Coupled Model Intercomparison Project Phase 5 and 6 (CMIP5, CMIP6)~~. Our model considers ~~takes into consideration of~~ phase change processes of soil pore water, thermal ~~property~~ properties difference between frozen and thawed soil, geothermal flux flow, and ground ice effect. The results indicate that 1) our model can consistently reproduce the vertical ground temperature profiles and active layer thickness (ALT), is superior in recognizing permafrost boundaries, and would realistically capture the evolution of the permafrost thermal regime, 2) spatial distribution of permafrost and its thermal conditions over the study area were controlled by elevation~~al~~ with a strong influence of slope ~~aspects~~orientation, 3) from 1970 to 2019, the regional averaged means annual ground temperature (MAGT) had warmed by 0.49 ℃ in the continuous permafrost zone and 0.40 ℃ in the discontinuous permafrost zone~~, . and t~~The lowest elevation of the permafrost boundary (on the north–facing slopes) rose approximately 47 m, a~~s well as~~nd the northern boundary of discontinuous permafrost has approximately retreated southwards 1~2 km, while the lowest elevation of the permafrost boundary remains unchanged for the continuous permafrost zone, 4) the warming rate in MAGT is projected to be ~~slighter higher~~more pronounced under Shared Socioeconomic Pathways (SSPs) than that of Representative Concentration Pathways (RCPs), but no distinct discrepancies in the areal extent of the continuous, discontinuous permafrost and seasonally frozen ground among SSP and RCP scenarios. This study highlights the slow delaying process in the response of mountain permafrost to a warming climate, especially in terms of the areal extent of permafrost distribution.

1 Introduction

Permafrost is one of the crucial components of the cryosphere that is sensitive to climate changes (Li et al., 2008; Nitze et al.,2018; Smith et al., 2022). Owing to its high elevation (mean elevation above 4000 m above sea level (a.s.l.)) and extreme cold climate, the ~~Qinghai–Tibet Plateau (~~QTP~~)~~ is the largest and highest elevational permafrost region (occupies a permafrost area of 1.06×10^6 km^2 or 40 % of the total area of the QTP) in the mid– to low– latitude regions ~~on earth~~ (Zhou et al., 2000; Yang et al., 2010; Zou et al., 2017; Zhao et al., 2020). Since the 20th century, climatic warming has been evident on the QTP, particularly in the permafrost regions, which has significantly impacted the permafrost, manifested by rising ground temperatures, ~~increasing~~

设置了格式: 上标

increase in ALT, thinning of permafrost, melting of ground ice, and disappearing of permafrost ultimately (Wang et al., 2000; Cheng and Wu, 2007; Wu et al.,2008; Jin et al., 2011; Li et al., 2012; Zhao et al., 2020; Zhang et al., 2021). Changes in the permafrost ~~conditions~~ e have substantial impacts on the hydrological process (Cheng et al., 2013; Zhao et al., 2019), the energy exchange between land and atmosphere (Xiao et al., 2013; Hu et al., 2017), natural hazards (Hjort et al., 2022), carbon budgets (Schädel et al., 2016; Miner et al.,2022; Hjort et al., 2022; Fewster et al., 2022), and ecological environments (Yi et al., 2014; Jin et al., 2021). Therefore, it has become an ~~imperative~~ pressing issue for ~~of~~ research ~~programs on climate change impact~~ to diagnose how and at what rate permafrost respond~~s~~ to global warming~~, accurately, and it~~ It has prompted a great concern ~~of~~ among geocryologists, cold regions engineers, and international society (IPCC, 2019).

The northern fringe on the continuous permafrost zone of QTP is exceptionally vulnerable to climatic variability, as characterized by permafrost and seasonally frozen ground coexistence, and a thicker active layer, much thinner and warmer permafrost in this region compared with permafrost in the interior of the QTP (Wu et al., 2005; Liu et al., 2020). Given the location of the northern lower limit of the continuous permafrost zone ~~on~~ of the QTP, ~~and on the other hand,~~ detailed permafrost environmental investigation and monitoring ~~here~~ have been ~~systematically~~ conducted since 1987 (Zhao et al., 2021)~~, and~~. A new ~~information on~~ dataset from remote sensing ~~spatial~~ products with a high resolution (e.g., Zou et al., 2014, 2017; Li et al., 2015b) is readily available ~~so that,~~ the Xidatan constitutes an ideal region to assess the response of marginal permafrost to a warming climate. To aid infrastructure construction of the Qinghai ~~Tibetan~~Tibet Highway (QTH), ~~some~~ multiple field investigations and borehole monitoring started in the late 1960s, documenting that ~~and documented~~ warming and thawing of permafrost have been striking in this study region (Jin et al., 2000, 2006; Cheng et al., 2007). ~~However, t~~There is little knowledge about the spatial variations, owing to the costly and challenging logistics of borehole installation in some remote areas (e.g., remote alpine mountain areas with steep and complex topography). ~~Moreover, t~~The high spatial heterogeneity (e.g., permafrost and seasonally frozen ground coexist) ~~in parameters~~ strongly influenced permafrost distribution (Cheng et al., 2004)~~. A~~ and a simple point observation to represent~~ing~~ regional conditions is problematic. Therefore, it is ~~hard~~ difficult to ~~be accurately delineated the margin of the permafrost distribution by traditional cartographic techniques based on the limited field survey data,~~

~~aerial photographs, satellite images as well as~~ accurately delineate the permafrost distribution margin by traditional cartographic techniques based on the limited field survey data, aerial photographs, satellite images, and topographic features dataset (Ran et al., 2012; Zou et al., 2017). It ~~highlight~~highlights~~ed~~ the demand for a spatial study approach to achieve a realistic picture of permafrost distribution for further study of thermal state and dynamics in response to climate ~~the demand for a spatial study approach to achieve a realistic picture of permafrost distribution for further study of thermal state and dynamics in response to climate variability.~~

~~Models~~variability. Models have the potential to overcome the shortage of in~~-~~situ ~~monitoring~~ and field surveying in mapping permafrost conditions and change studies (Riseborough et al., 2008). A variety of models can be applied ~~to~~ for the quantitative assessment of the response of marginal permafrost to the warming climate (Cheng et al., 1984; Li et al., 2008; Lawrence et al., 2012; Guo et al., 2016; Lu et al., 2017; Chang et al., 2018; Wang et al., 2019; Ni et al., 2021). However, most models are poor at interpreting marginal permafrost, especially true in the region of northern or southern permafrost boundaries, such as the Xidatan. ~~This~~Such challenges, in part, ~~is~~ are attributed to the effect of local factors (e.g., topography, vegetation, snow cover, ~~and~~ thermal properties of the surface soil, etc.). Near the lower limit of permafrost, the permafrost and seasonally frozen ground coexist. High spatial heterogeneities of the land surface make it a challenging area for permafrost modeling (Cheng et al., 2004; Zou et al., 2017, Luo et al., 2018; Yin et al., 2021). ~~Moreover, d~~Due to the lack of detailed field observations, most ~~of the~~ existing simulation results have not considered the effects of water phase change and ~~historical climate~~ground ice ~~as well as~~and the thermal state of deep permafrost. Hence, there is a considerable discrepancy among their results on the timing, rate, and magnitude of permafrost degradation (Zhao et al., 2020; Smith et al., 2022). ~~Which hardly makes us agree on a quantitative assessment of the response of marginal permafrost to the warm climate change~~. To address these issues, Sun et al. (2019) ~~established~~ proposed a transient numerical heat conduction permafrost model ~~in previous works, and it has~~ successfully simulat~~inged~~ the evolution ~~process~~ and dynamics of the permafrost thermal regime from 1962 until the end of this century at a monitoring borehole (QT09) located in the Xidatan comprehensive observation site.

In this work, we ~~try~~ attempt to upscale our model ~~to whole areas~~for the whole region, aiming

to accurately simulate mountain permafrost spatial distribution and dynamics.~~,~~ ~~aiming to accurately simulate the spatial distribution and dynamics of mountain permafrost~~ The objective includes the production of high ~~at a~~ resolution ~~of~~ 1 km×1 km, data~~,~~ for the current period of 1970–2019, and anticipate possible changes by 2100 under different climate change scenarios, forced by improved remote sensing-based spatial product (LST), and CMIP5 (under RCP 2.6, RCP4.5 and RCP8.5) and CMIP6 (under SSP1–2.6, SSP2–4.5, and SSP5–8.5) ~~climate~~ projections. Our model fully considers ~~gives full consideration to~~ the thermal properties~~y~~ difference between frozen and thawed soil, the phase variations of the unfrozen water in frozen soil, the distribution of the ground ice, and geothermal heat flow. ~~The model results were validated against considerable long-term continuous monitoring of soil temperatures at various depths, ALT, and observed permafrost distribution of boreholes as well as three existing permafrost distribution maps investigated in 1975, 2012, and 2016. Furthermore, changes in continuous and discontinuous permafrost zone in terms of the areal extent, northern boundary, and lower limits are analyzed first, and its characteristics (MAGT, permafrost table, permafrost base, and permafrost thickness) variation were investigated subsequently. Moreover, what is the difference in responses of continuous and discontinuous permafrost zone to climate change will also be discussed.~~ We ~~expect~~ aim that this study will simulate the distribution of marginal permafrost on the QTP, quantitatively assess the thermal regime spatiotemporal dynamics under climate change, and anticipate changes for future climate scenarios. ~~can realistically simulate the distribution of marginal permafrost on the QTP and quantitatively assess spatiotemporal dynamics of the thermal regime under current climate change, and reasonably anticipate possible changes for future diffident climate scenarios.~~ The findings are fundamental prerequisites for a ~~further~~ reasonable understanding of the patterns and processes of permafrost degradation on a hinterland QTP or global scale, thus supporting policy–makers, ~~the public,~~ and researchers to develop strategies for the cold regions in environmental management, hazard mitigation, adaptation, stability of engineering foundations design, conservation of land and water resources, etc.

2 Study area, materials and methods

2.1 Study area

The study focuses on the Xidatan of QTP, situated in a narrow down–faulted basin at the northern foot of the Eastern Kunlun Mountains within the northern limit of the permafrost on the QTP (Fig. 1a). The region encompasses a land area of ~220 km^2 and is characterized by discontinuous permafrost (Wu et al., 2005; Liu et al., 2020; Yin et al., 2021). Some periglacial landforms such as block fields, stripes, and stone rings have developed in the mountainous terrain (Luo et al., 2018~~), ,)~~. Several glaciers extend from the peaks of the East Kunlun Mountains downwards along the valley in the southern area (Fig. 1b) ~~and several glaciers extend from the peaks of the East Kunlun Mountains downwards along the valley in the southern area (Fig. 1b).~~ The elevation varies from 4100 m a.s.l. in the east to 5700 m a.s.l. in the west.~~The elevation varies from 4100 m a.s.l. in the east to 5700 m a.s.l. in the west, and t~~ Topographic relief in the majority (~90 %) is minimal (slopes lower than 5°) with some exceptions in mountainous areas. The plant community composition is mainly dominated by sparse alpine steppe, and the alpine desert consists of ~~more than~~> 10 m thick soil layer of gravel, fluvial sand, and silt (Wang et al., 2000; Jin et al., 2000; Yue et al., 2013; Yin et al., 2021)~~, but most parts of the ground surface are dry and almost barren~~ (Fig. 1b–g). According to ~~the observations in~~ the comprehensive ~~experimental~~ observation site (COS) ~~station~~ (Fig. 1b), from 2004 to 2018, the mean annual air temperature and mean annual precipitation were -3.6 °C and 384.5 mm, respectively~~.~~. In 2017, permafrost thickness was approximately 26 m, with the MAGT at zero annual amplitude (ZAA, where the annual difference in ground temperature is less than 0.1 ℃) was approximately -0.66 ℃ and ALT is about 1.60 m (Zhao et al., 2021).~~and in 2017, permafrost thickness was approximately 26 m, with the MAGT at the depths of zero annual amplitude (ZAA, where the annual difference in ground temperature is less than 0.1 °C) was approximately -0.66 °C, and ALT is about 1.60 m (Zhao et al., 2021).~~

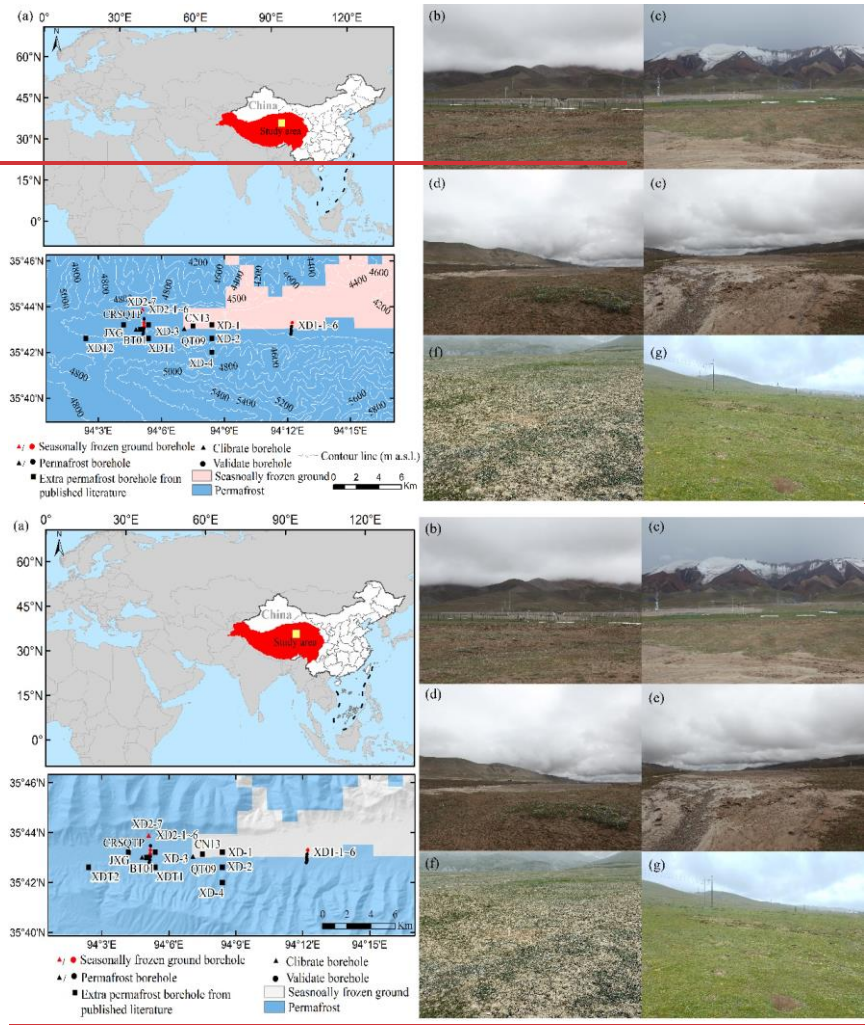

Figure 1. ~~Geographical~~ The ~~location~~geographical location of the Xidatan on the QTP, and its topography ~~as well as~~, and the location of 24 borehole sites (a). Surface condition at monitoring borehole sites ~~in the study area~~ (b–g): view over the Xidatan comprehensive observation site (b), QT09, view towards the south~~ern~~ (c), QT09, view towards the northeast (d), view from the vicinity of QT09 towards the east (e), XD2–1~2–7, view towards the south (f), XD1–1~1–6, view towards the east (g) (the spatial distribution of ~~permafrost~~ frozen ground types are~~is~~ derived from Zou et al. (2017); ~~contour line elevations~~topography ~~were~~ was generated ~~from~~ by the Digital Elevation Model constructed (DEM) from the Shuttle Radar Topography Missions (SRTM) with a 1-arcsecond (~30 m) (Jarvis et al., 2008), all photographs were taken during the field investigation from

23 Jul. 2021 to 2 Aug. 2021).

2.2 Materials

2.2.1 Field monitoring and borehole observation datasets

There are fifteen monitoring boreholes with long–term (for the last 10 years) ~~temperature~~ observations established in the Xidatan (Fig. 1a). A ~~comprehensive experimental station~~ COS ~~is located in~~is in the central part of the Xidatan, where the ground surface is composed of sparse dry alpine meadows ~~with numerous bared areas~~, and the soil layer is made of fluvial sand and gravel (Fig. 1b). A monitoring borehole QT09 (30 m in deep at 4538 m a.s.l.) and an automatic weather station (AWS) ~~had~~ automatically recorded long–term observed basic meteorological elements (May. 2004–Dec. 2018~~),), the soil moisture content in the active layer (Oct. 2009–Dec. 2018), and soil temperature at various depths (Jan. 2005–Dec. 2017).~~ Approximately 4 km from the ~~comprehensive experimental station~~COS, another 30 m ~~depth~~ deep borehole BT01 (4530 m a.s.l.) was drilled in sparse dry steppe with considerable coarse sand and gravel ~~on the surface~~, where the continuous soil temperature measurements were taken ~~continuously~~ at depths of 0.5 to 30 m span from 2004 to 2017. In these two sites, the soil moisture content in shallow layers (<1.1 m) ~~observed~~ ranged from 15 to 39 % and from 4 to 15 %, respectively, and the organic matter content of 4.2 % and 1.68 %, respectively (Liu et al., 2020).

In addition, during August 2012, thirteen boreholes from 8 to 15 m ~~in~~ depth (XD1–1~XD1–6, XD2–1~XD2–7) were drilled along parallel altitudinal transects at the east (3.15 km length) and west (3.86 km length) part of the Xidatan in ~~Aug. 2012~~ (Luo et al., 2018). The soil temperature records are available at ~~thirteen~~ these borehole locations ~~covering~~ covering November ~~the period Nov.~~ 2012 to ~~Sept.~~September 2017. The six boreholes (XD1–1~XD1–6) ~~exist~~ are located in dry and sparse grassland on the eastern altitudinal transect between 4368 m a.s.l. and 4380 m a.s.l. (Fig. 1g), among which the XD1–1~XD1–4 boreholes are all 15 m ~~in~~ deep, and the two other boreholes (XD1–5~XD1–6) are 8 m ~~in depth~~deep. A frozen layer has been observed in the five uppermost boreholes (XD1–1~XD1–5) while it was absent in the lowermost borehole XD1–6 (Luo et al., 2018). Similarly, seven boreholes were drilled at the western side of the Xidatan, resulting in an altitudinal transect from 4490 m a.s.l. (on the north) down to 4507 m a.s.l. (on the south). The first three boreholes

(XD2–1 to XD2–3) and XD2–6 are 15 m deep in sparse grassland. Similarly, boreholes XD2–4, XD2–5, and XD2–7, are 15 m, 15 m, and 8 m deep and located in river erosion-induced sand-rich sediment (Fig. 1e).~~The first three boreholes XD2–1 to XD2–3 as well as XD2–6 borehole were drilled 15 m into sparse grassland while river erosion area in the sand–rich sediment at boreholes XD2–4, XD2–5, and XD2–7, with 15 m, 15 m, and 8 m in depth, respectively (Fig. 1e)~~. The ground temperature monitoring results showed that permafrost existed in boreholes XD2–1 to XD2–3 and XD2–6, but there is no permafrost in boreholes XD2–4 to XD2–5 and XD2–7 (Luo et al., 2018; Yin et al., 2021).

The air temperature (height of 2, 5, and 10 m) and the volumetric unfroze soil water content in the active layer ~~data~~ were recorded, ~~respectively,~~ by a CR1000/CR3000 data acquisition instrument (Campbell Scientific Inc., USA, with ± 0.5 °C accuracy), and by a hydra–soil moisture sensor connecting to a CR1000 datalogger (Campbell Scientific, USA, with an accuracy of ± 2.5 %). A cable equipped with 20 to 30 high accuracy (± 0.1 °C) thermistors (SKLFSE, CAREERI, CAS) chain is connected to a CR3000/CR1000 (Campbell Scientific, Logan, UT, USA) data loggers and vertically arranged at depths from 0 to 30 m (the depths are not the same for all sites, details ~~see~~ are given Table A1). The ground temperature has been recorded automatically every 1 or 4 h at different ~~horizons~~depths. For more detailed description of the dataset as well as the thermistor set up and installations can be found in Luo et al. (2018) and Zhao et al. (2021). Before further proceeding, ~~the values which are clearly an~~ errors in the sensor were identified and ~~cleared~~fixed, and the outliers were replaced with valued generated by the data before and after (see Zhao et al. (2021) for more details on the quality control procedures). Then, the data ~~are~~ were re–sampled for the daily average and used to calibrate and validate the model performance. The spatial distribution of these borehole sites is displayed in Fig. 1a, and the crucial information about these boreholes employed for model calibration and validation is summarized in Table 1.

~~**Table 1. A list of monitoring boreholes in the study area and a summary of the ground properties are shown.**~~

~~Borehole (altitude/ m a.s.l.)~~	~~Coordinates~~	~~Sensor depths (m)~~	~~Frozen ground type~~	~~Soil stratigraphy~~

QT09 (4538)	35°43′02″ 94°07′05″	0.5–5 m (0.5 m intervals) 5–20 m (1 m intervals) 20–30 m (2 m intervals)	Permafrost	Loam (0–0.2 m) Sandy loam (0.2–1.4 m) Sandy loam with gravel (1.4–2.4m) Sandy with gravel (2.4–10 m) Rock (10–21 m)
TB01 (4530)	35°43′00″ 94°04′09″	Same as QT09	Permafrost	Sandy loam (0–1.2 m) Sand (1.3–3 m) Sand with gravel (3–10 m) Weathered mudstone (>10 m)
XD1–1 (4379)	35°41′55″ 94°12′05″	0.5–10 m (0.5 m intervals) 10–15 m (1 m intervals)	Permafrost	Sandy cobble (0–4.5 m) Fluvial sand (4.5–15 m)
XD1–2 (4377)	35°41′59″ 94°12′07″	Same as XD1–1	Permafrost	Sandy cobble (0–4.5 m) Fluvial sand (4.5–15 m)
XD1–3 (4576)	35°42′04″ 94°12′07″	Same as XD1–1	Permafrost	Sandy cobble (0–5 m) Fluvial sand (5–15 m)
XD1–4 (4374)	35°42′10″ 94°12′07″	Same as XD1–1	Permafrost	Sandy cobble (0–5.5 m) Fluvial sand (5.5–15 m)
XD1–5 (4370)	35°42′16″ 94°12′08″	0.5–8 m (0.5 m intervals)	Permafrost	Sandy cobble (0–5.5 m) Fluvial sand (5.5–10 m)
XD1–6 (4368)	35°42′24″ 94°12′09″	Same as XD1–5	Seasonally frozen ground	Sandy cobble (0–4.5 m) Fluvial sand (4.5–8 m)
XD2–1 (4508)	35°41′56″ 94°05′08″	Same as XD1–1	Permafrost	Sand (0–2.5 m) Sand with massive ground ice (2.5–7 m) Clay (7–9 m) Weathered mudstone (9–15 m)
XD2–2 (4503)	35°42′01″ 94°05′09″	Same as XD1–1	Permafrost	Sand (0–2.8m) Sand with massive ground ice (2.5–6 m) Weathered mudstone (6–15 m)
XD2–3 (4500)	35°42′10″ 94°05′09″	Same as XD1–1	Permafrost	Sand cobble (0–4 m) Fluvial sand (4–15 m)
XD2–4 (4498)	35°42′18″ 94°05′09″	Same as XD1–1	Seasonally frozen ground	Sandy cobble (0–4 m) Fluvial sand (4–15 m)
XD2–5 (4493)	35°42′26″ 94°05′10″	Same as XD1–1	Seasonally frozen ground	Sandy cobble (0–4 m) Fluvial sand (4–15 m)
XD2–6 (4490)	35°42′36″ 94°05′11″	Same as XD1–1	Permafrost	Sandy cobble (0–4 m) Fluvial sand (4–15 m)
XD2–7 (4492)	35°43′00″ 94°05′05″	Same as XD1–5	Seasonally frozen ground	Sand (0–4.5 m) Sandstone (4–8 m)
JXG (4530)	35°43′12″ 94°04′01	1–10 m (1 m intervals) 10–30 m (2 m intervals) 0.4 m 1.6 m	Permafrost	—
CRSQTP (4530)	35°43′ 94°05′	4–10 m (2 m intervals) 10–18 m (4 m intervals) 18–20 m (2 m intervals) 20–29 m (3 m intervals)	Permafrost	—
XD1 (4427)	35°43′12″ 94°08′24″	—	Permafrost	—
XD2 (4530)	35°43′12″ 94°04′14″	—	Permafrost	—
XD3 (4480)	35°43′12″ 94°05′24″	—	Permafrost	—
XD4 (4427)	35°42′00″ 94°08′24″	—	Permafrost	—
XDT1 (4602)	35°42′36″ 94°02′24″	—	Permafrost	—
XDT2	35°42′36″	—	Permafrost	—

(4530)	94°05′24″			
CN13 (4448)	35°42′12″ 94°07′48″	—	Permafrost	—

Note: The symbol is field-observed frozen ground types collected from previously published literature (Wang et al., 2000; Jin et al., 2000,2006; Cheng et al., 2007).

Table 2. Calibration thermophysical parameters of different soil layers used for soil temperature modeling. Soil texture information from Luo et al. (2018) and Liu et al. (2021), the values of thermal conductivity and heat capacity were from Construction of Ministry of PRC. (2011) and Yershov. (2016), and fine-adjusted during the calibration, water content was determined by the soil samples of the borehole cores combined with the observation dataset vicinity of QT09 and the ground ice distribution maps from Zhao et al. (2010).

Texture	*K* (W m^{-1} °C^{-1})		*C* (kJ m^{-3} °C^{-1})		VWC (%)
	Frozen	Thawed	Frozen	Thawed	
Loam	1.25–1.57	0.85–1.28	1639–1879	2208–2475	15–20
Clay	0.83–1.30	0.61–1.03	1756–1907	1881–2191	15–20
Sandy loam	1.31–1.93	1.17–1.71	1844–2107	2258–2634	10–20
Loamy sand	1.02–1.38	1.11–1.24	2040–2208	2541–2676	15–20
Sand cobble	1.0–1.29	0.89–1.10	1639–1739	2007–2208	13–15
Fluvial sand	1.32–1.60	1.09–1.30	1288–1413	1568–1819	6–10
Sand	1.86–2.15	1.48–1.64	1505–1639	1940–2208.1	10–14
Sandstone	0.94–1.91	0.77–1.47	1317–1459	1493–1777	2–6
Sand with Gravel	1.91–2.20	1.47–1.68	1459–1601	1777–2061	6–10
Weathered mudstone	2.27	1.71	1543	1881	6
Rock	0.33	0.33	1940	1940	2

Note: *K* is the thermal conductivity; *C* is the volumetric heat capacity; as well as *VWC* represents total volumetric water/ice content.

2.2.2 Official mMeteorological observations from Chinses Meteorological Administration

The observed temperature dataset from China Meteorological Administration (CMA) ground–based meteorological stations were was used to extend the land surface temperature (LST) series since the 1970s. For that, observed daily mean air temperature data for the 1970 to 2019 period at two AWS of CMA nearby (Wudaoliang:35°13′ N, 93°05′ E and Golmud:36°25′ N, 94°55′ E) was

downloaded from China Meteorological Data Sharing Service System (http://data.cma.cn/).

2.2.3 Remotely sensed land surface temperature datasets

Modified Moderate Resolution Imaging Spectroradiometers Land Surface Temperature (MODIS LST) product is used to force transient heat flow model ~~at~~ for spatial~~ly~~ modeling of alpine permafrost distribution. The MODIS onboard the Terra and Aqua satellites have provided LST measurements at a spatial resolution of 1 km×1 km since 2003~~, respectively~~ (https://modis.gsfc.nasa.gov/). Here, we employ clear–sky MOD11A2 (Terra MODIS) and MYD11A2 (Aqua MODIS) products (processing version 6), which contain two night–time measurements per day for the same pixel (Zou et al., 2017). Before proceeding, time series of irregularly spaced observations owing to clouds or other factors were identified, and gaps were filled by the Harmonic Analysis Time-Series (HANTS) algorithm (Obu et al.,2019). ~~And a~~An empirical model (Zou et al.,2014, 2017) was subsequently established to get mean daily values from Aqua and Terra daytime and night time transient LST~~time transient LST, and~~. ~~the~~ The model validation ~~showed perfect well~~was perferct over the Xidatan, with the square of the correlation coefficients R^2 above 0.9, $P<0.01$. Details of these algorithms can be found in Xu et al. (2013) and Zou et al. (2014).

2.2.4 Additional validation datasets

The comprehensive investigation of permafrost and its environments in the Xidatan~~ has been~~ was conducted in 1975 and 2012, respectively (Nan et al., 2003; Luo et al., 2018). The lowest elevation of permafrost boundary in 1975 and 2012 was approximately 4360 m a.s.l and 4388 m a.s.l., respectively, by ground–penetrating radar (GPR) profiles combined with drilling boreholes. Subsequently, permafrost distribution in this region was delineated on a topographic map at a scale of 1:50000~~, by hand empirically~~ using contour elevations ~~line on the basis of~~based on the field survey data, aerial photographs, and satellite images (Fig. 6a–b). In addition, one benchmark map of permafrost distribution in 2016 was accomplished by Zou et al. (2017)~~, which is~~ simulated by the temperature at the top of the permafrost (TTOP) model (Fig. 6c). The abovementioned three maps were used as the validation data to evaluate model performance in ~~the distribution of permafrost~~ permafrost distribution. Furthermore, the long–term continuous ALT observed dataset in the BT01, QT09, XD–1, XD2–4, and XD2–6 interpolated from the in–situ soil temperature profile (Liu et al.,

2020; Yin et al., 2021) were also used to evaluate the model performance. Moreover, the observed permafrost distribution of boreholes (CRSQTP, JXG, XD1, XD2, XD3, XD4, XDT1, XDT2, CN13) was used to assist in determining whether permafrost exists or not.

2.3 Methods

2.3.1 Model description

We simulated the subsurface temperature dynamics along the soil column by numerically solving the one–dimensional transient Fourier's law heat conduction equation. The physical basis and operational details of the model are documented in Sun et al. (2019), and only a brief overview of the model properties for a single grid cell is given here. Ground temperature T changes over time t and depth Z through heat conduction, as described by:~~:~~

$$C_{eff}(z,T)\frac{\partial T}{\partial t}-\frac{\partial}{\partial z}\left(k(z,T)\frac{\partial T}{\partial z}\right)=0 \quad (1)$$

A constant geothermal heat flow of Q_{geo}=0.08 W m^{-2} (Wu et al., 2010) as the lower boundary condition, and LST as the upper boundary condition. The thermal properties of the ground are described in terms of heat capacity C, thermal conductivity k and total volumetric water/ice content VWC. The latent heat effects of the water–ice phase transition ~~is~~ are accounted for in terms of an effective heat capacity $C_{eff}(z, T)$. The heat transfer equation (Eq.1) was discretized along with a soil domain to 100 m depth using finite differences, Subsequently, the trapezoidal rule was applied ~~and subsequently applied the trapezoidal rule~~ to numerically solve moderately stiff ordinary differential equations (Schiesser, 1991; Westermann et al., 2013). With comprehensive consideration of the modeling precision and computation cost, we choose the calculate time step to be one day, and set a total of 282 vertical levels for each soil column, with the vertical resolution configurations of 0.05m (the upper 4 m) and 0.5m (remaining soil layer to 100 m).

2.3.2 Model calibration and validation

We selected four borehole sets (Fig. 1a), which represented different soil type classes with various thermal properties for the initial model calibration, and the remaining sites for cross-

validation. The sites were selected based ~~Based~~ on surface deposits ~~and~~ , vegetation coverage, and a soil type maps at an 1 km×1 km spatial resolution ~~identified by satellite images as well as surficial soil type map at a 1 km spatial resolution~~ (Li et al., 2015b, Luo et al., 2018), ~~we selected four borehole sets (Fig. 1a), which represented different soil type classes with various thermal properties for the initial model calibration, and the remaining sites for cross–validation.~~ Thermophysical properties (e.g., stratigraphies, texture, ground ice content, ~~and~~ organic matter content, dry bulk density) of distinct soil layers were measured or assessed from field surveys, laboratory and on–site measurements, as ~~well as~~nd tests ~~on~~ of soil samples obtained from fifteen borehole cores (depths between 8~30 m). These boreholes were specific for each soil class and geographical location. The detailed information about test methods for the bulk density, and moisture content of soil sample, readers are ~~kindly~~ referred to Zhao et al. (2015). Furthermore, a time series of observed soil water content dataset in the active layer (Sun et al., 2019, 2022; Zhao et al., 2021) vicinity of the site (QT09) and the ground ice distribution maps accomplished by Zhao et al. (2010) ~~are~~ is used ~~served as~~ for water content estimated of each soil type. And then, ~~Based on the above properties,~~ we pre–selected narrow ranges of plausible values of typical soil thermophysical parameters (thermal conductivity and heat capacity), and fine–adjusted during model calibration~~. As suggested by Hipp et al. (2012),~~ The a manual, stepwise optimization procedure was used to adjust parameters based on the suggestion by Hipp et al. (2012). Specifically, calibration was performed firstly by systematically changing *k* over the given plausible ranges improve ~~aiming for improving~~ the agreement between the simulated and observed ground temperature at different depth levels. Subsequently, minor adjustments were made to *C* to promote the model performance.

~~After selecting the appropriate parameters, to estimate a realistic initial temperature profile before subsequent modeling, t~~The model was initialized by cyclical forcing of ~~at~~ the first ~~one~~ year LST data ~~of cyclical forcing~~ until the soil temperature profile reached a steady state to estimate an initial temperature profile. The number of spin–up cycles was between 2000 to 3300, and the criterion of soil temperature profile reached equilibrium under the upper and lower boundary condition was set at less than 0.0001 ℃/cycle. The ~~ground temperature profile of the last day subsequently was~~ last-day ground temperature profile was subsequently used as the initial condition for subsequent modeling.

设置了格式: 字体颜色: 文字 1

带格式的: 缩进: 左侧: 0.74 厘米

The agreement between the model grid and borehole monitoring site was quantified at each depth in terms of the mean absolute error (MAE) and root mean square error (RMSE) (Willmott and Matsuura, 2005; Jafarov et al., 2012):

$$MAE=\frac{1}{n}\sum_{i=1}^{n}|Ob_i-Sm_i| \quad (2)$$

$$RMSE=\sqrt{\frac{\sum_{i=1}^{n}(Ob_i-Sm_i)^2}{n}} \quad (3)$$

where Ob_i, Sm_i is observation and simulation value, respectively. And n is the total amount of data. The *MAE* shows an overall error between observing and simulating when the *RMSE* emphasizes an error variation.

2.3.3 Historical and future long–term LST series

We extended LST by establishing ~~To extend the LST to an earlier period, we established~~ statistical relationships between local LST and air temperature (AT) from nearby AWS~~,~~. These were subsequently used to derive long–term historical and future LST series for each grid point from historical (1970–2019) AT observation and the multi-model ensemble AT projection by 2100 under different climate change scenarios. ~~which were subsequently used to derive long–term historical and future LST series for each grid point from historical (1970–2019) AT observation, and from the multi–model ensemble AT projection by 2100 under different climate change scenarios.~~

The AT_cma, AT, and LST denote the air temperature from the CMA, air temperature at 2 m ~~heights~~ from our ~~comprehensive experimental station~~COS, and ground surface temperature derived from modified MODIS LST, respectively. ~~There are three steps. 1)~~Firstly, we established linear regression between LST and AT from the measured period of 2004 to 2018, the temperature variability is highly correlated between LST and AT with R^2= 0.83 (~~significant at 0.05 level~~$P<0.01$), ~~2)~~ secondly, daily AT series from 1970 to 2019 were generated utilizing a stepwise linear regression between measured AT during 2004 to 2018 and those extracted from CMA meteorological stations (AT_cma) ~~at a~~ nearby, this procedure worked well with R^2 = 0.88 ($P<0.01$~~significant at 0.05 level~~).

设置了格式: 字体: 倾斜

3) ; In the third, we generated a time series of LST starting from 1970 based on the AT–LST linear regression model induced in step 1 and extending series AT in step 2, and we generated a time series of LST starting from 1970.

For future AT projections, the Sixth Assessment Report of IPCC the latest recent Intergovernmental Panel on Climate Change Work Group1 Sixth Assessment Report (Iturbide et al., 2020; IPCC, 2021) has evaluated and projected climate change over the QTP during the 21st century (https://interactive-atlas.ipcc.ch). The models estimated warming trends between 1995–2014 and 2081–2100, and suggest a gradual linear increase in mean annual AT in QTP under three RCPs scenarios are ofis 0.013 ℃ a^{-1} (RCP2.6, low concentration of emissions), 0.028 ℃ a^{-1} (RCP4.5, stable concentration of emissions) and 0.060 ℃ a^{-1} (RCP8.5, high concentration of emission), respectively, calculated frombased on the multi–model ensemble median (21–29 model outputs) of CMIP5. TAs regards newly designed SSP scenarios in CMIP6, the mean linear warming rate is 0.017 ℃ a^{-1} (SSP1–2.6, strong climate change mitigation), 0.032 ℃ a^{-1} (SSP2–4.5, moderate mitigation), and 0.064 ℃ a^{-1} (SSP5–8.5, no mitigation), respectively, estimated from CMIP6 ensemble median of 31–34 model outputs. Using the AT–LST linear regression relationship model again, we can obtained a mean LST warming rate of 0.012 (RCP2.6), 0.025 (RCP4.5), and 0.050 ℃ a^{-1} (RCP8), and a mean LST increase rate of 0.015 (SSP1–2.6), 0.030 (SSP4–4.5) and 0.057 ℃ a^{-1}(SSP5–8.5).

2.3.4 Spatially modeling

We used the calibrated model forced with extended and projected LST forForcing the calibrated model using extended and projected LST series, we simulating ed the spatial distribution of permafrost in the Xidatan. Like the setup of a single grid cell (Section 2.3.1), at each grid point, the ground thermal regime was simulated for a specific ground stratigraphy under boundary conditions using from a one–dimensional multilayer soil profile down to the depth of 100 m. Well–adjusted thermos–physical parameters of multilayered soil columns during the model calibration were specified and assigned for each grid cell of the same soil classes in the surrounding areas of the calibrating borehole. Based on the soil type map at 1km×1km spatial resolution (Li et al., 2015b), well–adjusted thermos–physical parameters of multilayered soil columns in section 2.3.2 were

specified and assigned for each soil type. If the maximum temperature of any soil layer in the grid point was ≤ 0°C for two consecutive years, the model cells were ~~designated~~ identified as permafrost. In contrast, the seasonally frozen ground was defined from the not–yet–assigned cells, in which the minimum soil temperature of any layer in the same two years was ≤ 0 °C. The remaining cells were ~~defined as~~ unfrozen ground (Wu et al., 2018). ~~Meanwhile, t~~The continuous permafrost zone is defined as the region where the area coverage of permafrost is more than 90 % (of the total accounts area). Otherwise, it was demarcated as a discontinuous permafrost zone (Qin et al., 2014).

~~In total, t~~The simulation domain comprises about 280 km^2 with a horizontal resolution of 1 km ×1 km, corresponding to 280 independent runs. ~~With comprehensive consideration of the modeling precision and computation cost, we choose the time step to be one day, and set a total of 282 vertical levels, with the vertical spatial resolution of 0.05 m (the upper 4 m) and 0.5 m (remaining soil layer to 100 m).~~

3 Result

3.1 Model ~~'s performance~~ evaluation

Simulated ground temperature r~~R~~esults demonstrate that relative larger bias~~es~~ (with the MAE ranging from 0.69 to 2.02 ℃ as well as RMSE ranging from 0.87 to 2.46 ℃) for surface soil layer to 1 m in depth ~~for shallow depth (below 1 m depth) ground temperature~~ at all calibration sites (Fig. 2), which can be explained by frequent fluctuation and complex variation pattern of ground temperature itself at shallow depth greatly affected by local factors (e.g., terrain, water bodies, snow cover, ~~and~~ vegetation, etc.). However, these discrepancies between simulated and observed ground temperature gradually reduce with the increase of soil depth. Most calibration boreholes showed a good correspondence between modelled and measured ground temperature at the intermediate (3 m, 8 m) and deep (15 m, 30 m) layers (Fig. 3), with an MAE of 0.05–0.52 ℃, 0.04–0.38 ℃, as well as an RMSE of 0.06 –0.58 ℃, 0.04–0.38 ℃, respectively. The same pattern appeared at validation sites (Fig. 4–5). Ground temperature in validation sites was equally well reproduced by the calibrated model, yielding an MAE of 0.86–1.27 ℃ (RMSE of 1.15–1.63 ℃) in the 0.5 and 1 m and 0.01–0.52 ℃ (RMSE of 0.08–0.80 ℃) in 3 and 15 m. ~~In general~~Generally, ~~very~~ consistent daily

fluctuations of the simulated and observed soil temperature at all observational depths for most calibration and validation sites, indicate the daily variation of the ground temperature field is ~~and indicate the daily variation of the ground temperature field is~~ simulated satisfactorily by our calibrated model.

Site XD2–6 has relatively poor performance in the deep layer (8 m and 15 m) compared with ~~other sites~~the shallow layers (fig). ~~It~~ It might be caused by micro-scale heterogeneity in terms of surface cover, topography, and soil stratigraphy at the sub-grid scale, leading to more difficulty in accurate modeling

~~It may be attributed to being located at the edge of the discontinuous permafrost zone, and the land surface exhibits high spatial heterogeneities, leading to more difficulty in accurate modeling.~~ Nevertheless, the deviation between the modelled results and measured values for this site is within 0.38 ℃ at the deep layer (15 m). Furthermore, permafrost was simulated to disappear in the mid–late 2010s, which is in line with the observation (Yin et al., 2021). ~~We can conclude that various depths of ground temperature simulated by our model are still satisfactory for this site.~~

带格式的: 缩进: 首行缩进: 0 字符

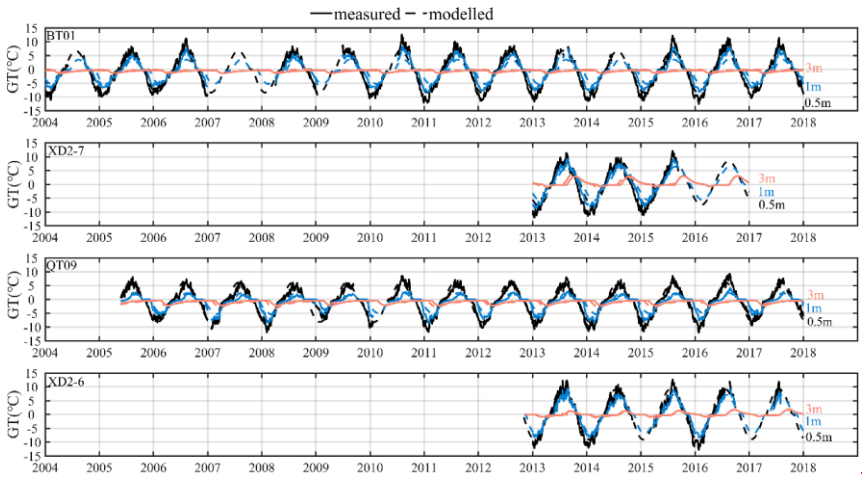

~~**Figure 2. Comparison of the simulated (dashed lines) to observed (solid lines) daily mean ground temperature (GT) at various depths (0.5 m: black, 1 m: blue, 3 m: brown) in four calibration boreholes (from the top to the bottom, each row shows the result at the BT01, XD2-7, QT09, and XD2-6, respectively) during the**~~

~~observation period (At the XD2–7 and XD2–6, observation data from 2004 to 2012 is not available, and 2013 to 2017 served comparison period, the BT01 and QT09 were compared during 2004–2017, and 2005–2017, respectively).~~

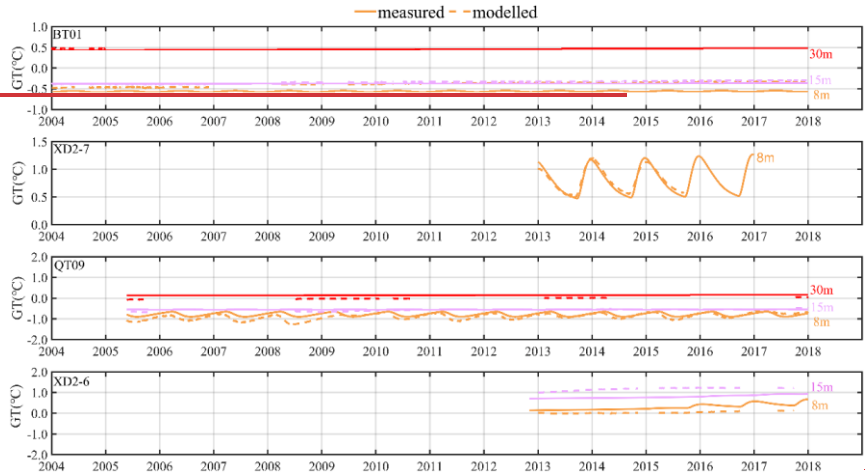

~~Figure 3. Same as Figure 2. but for daily mean soil temperature at 8 m (Orange), 15 m (magenta), 30 m (red).~~

~~Table 3. Error metrics for the assessment of daily average GT at different depths, which derived from the observed with simulated for individual calibration and validation site (good criteria values<0.2 °C are displayed in italics).~~

带格式的: 居中

Table 3. Error metrics for the assessment of daily average ground temperature at different depths, which derived from the observed with simulated for individual calibration and validation site (good criteria values<0.2 °C are displayed in italics).

Criteria	Site	0.5 m	1 m	3 m	8 m	15 m	30 m
MAE	BT01	1.04	1.04	0.52	0.41	*0.19*	*0.09*
(°C)	XD2-7	2.02	1.46	0.38	*0.05*		
	QT09	1.06	0.89	0.23	*0.16*	*0.18*	*0.04*
	XD2-6	1.42	0.69	0.23	0.22	0.38	
	XD2-1	1.05	0.95	0.41	*0.13*	*0.19*	
	XD2-4	1.01	0.86	0.21	*0.14*	*0.01*	

	XD1-1	1.27	1.18	0.52	0.25	*0.19*	
	XD1-4	1.11	0.92	0.44	*0.19*	*0.08*	
RMSE	BT01	1.36	1.38	0.72	0.41	*0.19*	*0.09*
(℃)	XD2-7	2.46	1.79	0.58	*0.06*		
	QT09	1.40	1.48	0.40	*0.17*	*0.18*	*0.04*
	XD2-6	1.78	0.87	0.30	0.23	0.38	
	XD2-1	1.36	1.20	0.54	0.24	*0.19*	
	XD2-4	1.31	1.15	0.35	*0.14*	*0.02*	
	XD1-1	1.63	1.48	0.80	0.25	*0.19*	
	XD1-4	1.41	1.19	0.62	0.20	*0.08*	

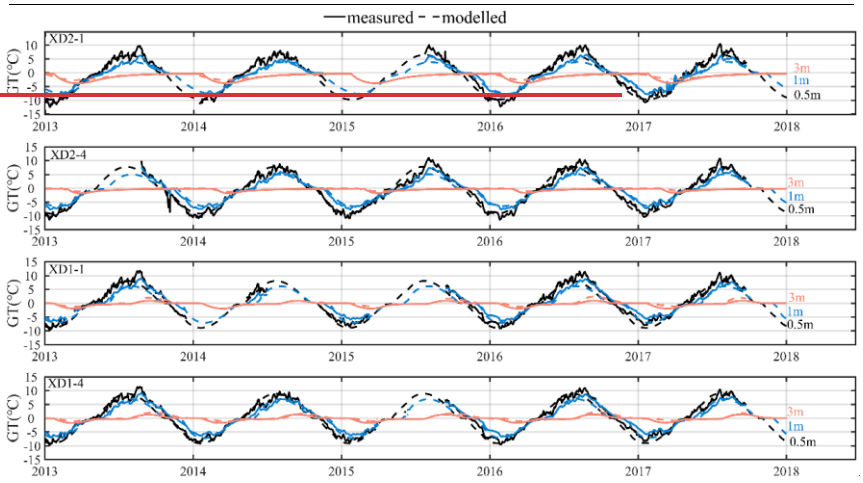

~~Figure 4. Comparison of simulated (dashed lines) to observed (solid lines) daily mean GT at various depths (0.5 m: black, 1 m: blue, 3 m: brown) in four validation boreholes (from the top to the bottom, each row shows the results at the XD2-1, XD2-4, XD1-1, and XD1-4, respectively) during the observation period from 2013 to 2017.~~

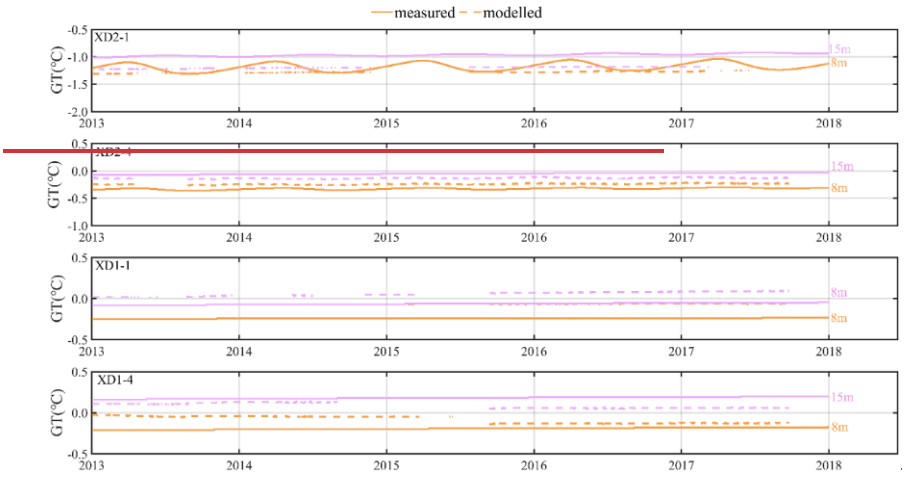

~~Figure 5. Same as Figure 4, but for daily mean soil temperature at 8 m (Orange), 15 m (magenta).~~

带格式的: 居中

To better estimate the model performance ~~on~~ in spatial modeling, we compared our simulations with three permafrost maps investigated in the 1975, 2012, and 2016. Based on the validation of the various maps against the permafrost and seasonally frozen ground observation at 24 boreholes (Fig. 6.), we found both 1975 and 2012 maps can well interpret~~ated~~ the relative continuous permafrost zone at the central–western Xidatan ~~above 4500 m a.s.l~~. However, there are many erroneous (12.5 % for 1975, and 16.6 % for 2012) recognitions of seasonally frozen ground at the discontinuous permafrost zone. It indicated that these two permafrost maps could not well represent the historical permafrost distribution status in the ~~where~~ permafrost and seasonally frozen ground coexist ~~, which is different from the investigated boreholes, and underestimated the permafrost area over this region.~~ In addition, these two maps are ~~alpine areas in the northeastern above 4200 m a.s.l. was uniformly identified as seasonally frozen ground, which is~~ strongly inconsistent in the regions of widespread seasonally frozen ground in the eastern border of our study region with the 2016 map and our simulations (Fig. 6a–b). The 2016 map and our simulations showed a very consistent pattern of permafrost distribution, and identified almost all locations of continuous permafrost correctly (Fig. 6c–f). However, the slight discrepancy existed between the 2016 map and our simulation in ~~had slight errors in both~~ permafrost (8.3 %) and seasonally frozen ground (8.3 %) locations over margins

of the discontinuous continuous permafrost zone~~,~~. Our simulate of the ~~whereas our simulation results recognized that~~ seasonally frozen ground distribution ~~exists~~ in this region~~.~~~~, which is consistent with the investigated results~~.

设置了格式: 英语(美国)

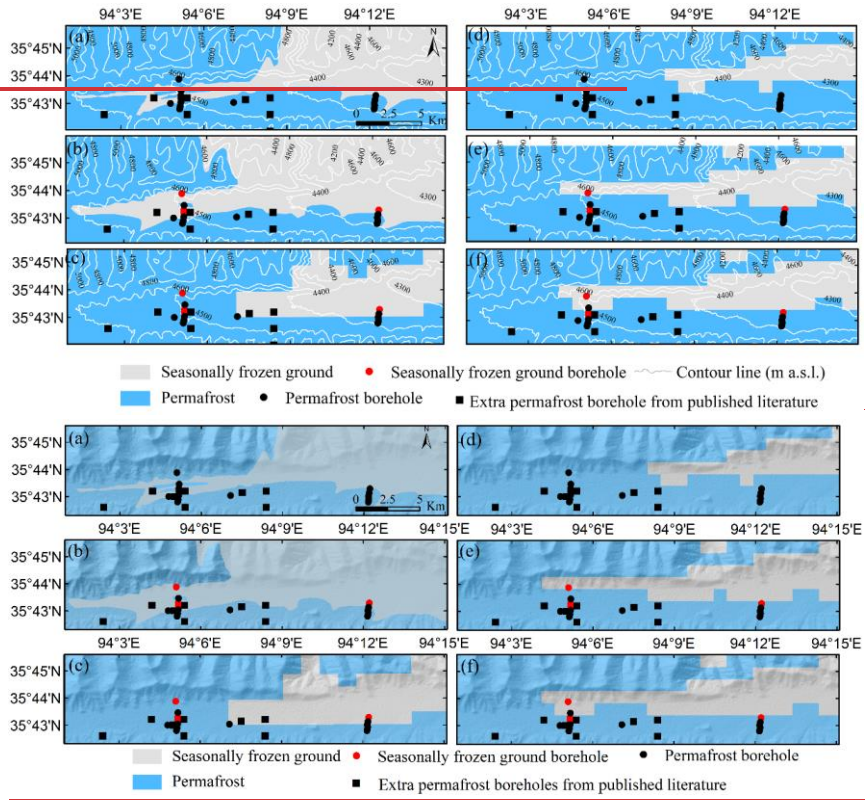

Figure 6. Geographic distribution of permafrost and seasonally frozen ground across the Xidatan for three permafrost maps accomplished in 1975, 2012 and 2016 (left panels 1975 (a), 2012 (b), 2016 (c), published in Nan et al. (2003), Luo et al. (2018) and Zou et al.(2017)) compared to corresponding modeled outputs (right panels, 1975 (d), 2012 (e), 2016 (f)).

~~The ALT is a critical index in understanding permafrost thermal state and dynamics.~~ Continuous multi-year ALTs derived from five monitoring sites were compared with those from the model-simulated (Fig. 3). The results indicated that there is a strong positive correlation between the simulated and observed ALT (R^2=0.98, P<0.01), and the simulation bias in the ALT from these

sites are within ± 0.25m. In terms of geographical structure, the spatial characteristics of ALT across the study area are well captured by our model. Both observed and simulated ALT in XD2–6 varied from 4.15 to 4.31 m, which is higher than other sites (BT01 of 2.55 to 2.85 m; the QT09 of 1.45 m to 1.60 m; the XD2–1 of 2.30 to 2.48 m; the XD2–3 of 2.95 to 3.05 m).

~~Continuous multi-year ALTs derived from monitoring sites were compared with those from the model-simulated (Fig. 7). Though some discrepancies between the measured and simulated ALT, overall, the value is very close to each other. Both observed and simulated ALT in the XD2–6 varied from 4.15 to 4.31 m, which is higher than that in other sites (the BT01 of 2.55 to 2.85 m; the QT09 of 1.45 m to 1.60 m; the XD2–1of 2.30 to 2.48 m; the XD2–3 of 2.95 to 3.05 m). The model has a good performance for ALT in the QBT01, QT09, XT2–1, as well as XD2–3, with an MAE of 0.03 to 0.07 m, and an RMSE of 0.04 to 0.09 m, respectively, but a relatively high error occurred at the XD2–6 (MAE of 0.15 m, RMSE of 0.19 m).~~

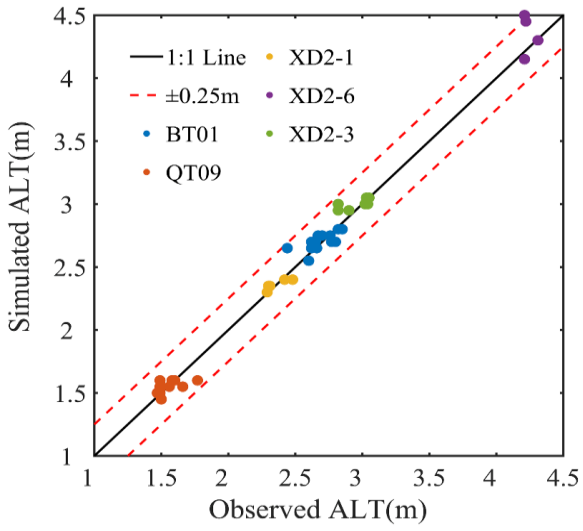

Figure 7. Comparison between annually observed ALT and simulated at different sites (the TB01 and QT09 (Liu et al. (2019), Zhao et al. (2021) observed from period 2005 to 2017, 2005 to 2018 are available, respectively, observation period at the XD2-1, XD2-3, and XD2-6 (Yin et al. (2021)) are from 2013 to 2019, 2013 to 2017, respectively. The solid line is a 1:1 line and the dashed line shows biases within ±0.25 m, dots are colored to represent the different sites).

3.2 Historical permafrost evolution

~~In this study, o~~Our simulation outputs were combine ~~together~~ with topographic data (elevation and slopes) derived from 30 m-DEM to analyze the permafrost distribution and its dynamics. ~~In addition,~~ MAGT at the depths of ZAA, permafrost table, permafrost base, and permafrost thickness are defined from temperature profiles, as critical parameters to describe the permafrost thermal regime, and were also chosen for analysis and discussion. Areas with seasonally frozen ground were excluded from the subsequent ~~following~~ studies.

3.2.1 Initial situation of permafrost distribution

The simulation results (Table 4–5, Fig. 8) showed the initial situation in 1970. The lower limit of continuous permafrost modeled was ca.4525 and 4732 m a.s.l., respectively, on the north–and south–facing slopes. While the lowest elevation of the permafrost boundary simulated was 4138 m a.s.l (on the north–facing slopes) and 4357 m a.s.l (on the south–facing slopes). A~~nd a~~pproximately 80 % of the total counting area was underlain by permafrost (33.93 % was continuous, and 46.07 % was discontinues) in the Xidatan. Regionally, the distribution characteristics of permafrost conditions are predominantly controlled by elevations. ~~In general, w~~ With altitude ascending westward gradually, permafrost temperature and permafrost table show a decreasing trend, whereas the position of permafrost base and permafrost thickness increase ~~display a decreasing trend, whereas the position of permafrost base and permafrost thickness show an increase~~. Furthermore, local topographic factors in t~~erms of~~ slope ~~aspect~~ also governed permafrost distribution in the study area. Permafrost temperature on the north–facing slopes were far colder than that of on south–facing slopes within the same elevations (Fig. 8a). ~~Specifically, on~~On the south–facing slopes (with high altitudes above 4500 m a.s.l.) and north–facing slopes model ~~presented~~ shows a comparatively cold permafrost temperature (MAGT ranges from -0.5 to -4.5 ℃), ~~and the permafrost table s~~Simulated permafrost table was less than 2.5 m, and permafrost base of 20 to 48 m as well as permafrost thickness of up to 46 m at the maximum. Whereas on south–facing slopes with low altitudes below 4500 m a.s.l., MAGT modeled is higher than -0.5 ℃, the position of the permafrost table modeled varies 2.5 to 4.5 m, permafrost base is at a depth of fewer than 20 m, and permafrost thickness of approximately 4 m at the thinnest.

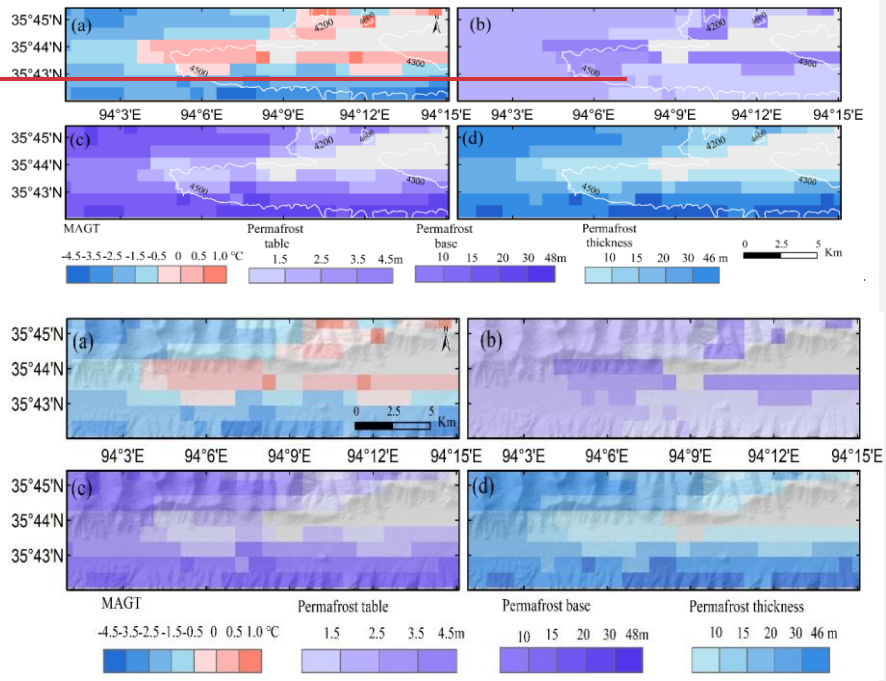

Figure 8. Spatial distributive features of MAGT (a), permafrost table (b), permafrost base (c), and permafrost thickness (d) for the initial simulation of the 1970s over the Xidatan (grey areas with the seasonally frozen ground were excluded).

3.2.2 Changes ~~in~~of permafrost conditions

From 1970 to 2019, the simulation results indicated that the lower limit of the continuous ~~permafrost zone remained unchanged over the study areas. The lowest~~ elevation of the permafrost boundary has a remarkable rise of 47 m on the north–facing slopes, while that remained unchanged on the south–facing slopes (Table 4). Correspondingly, around 12.86 % of the discontinuous permafrost zone has transformed into ~~the~~ seasonally frozen ground (Table 5), which caused the northern boundary of the discontinuous permafrost zone ~~having~~ to have approximately retreated southwards 1~2 km, but that is unchanged for the continuous permafrost zone (Fig. 9).

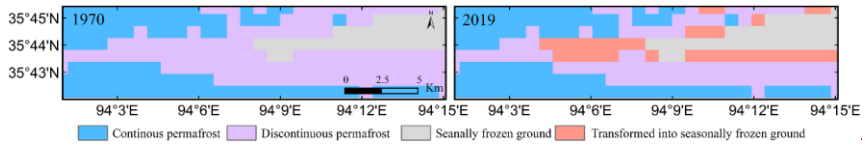

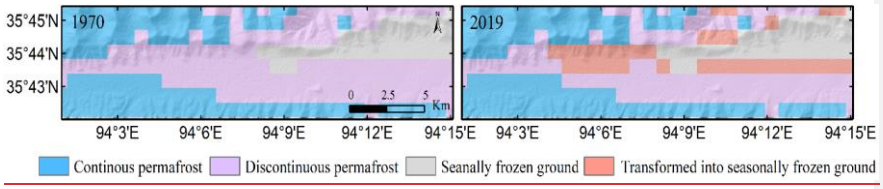

Figure 9. Spatial distributive changes of continuous and discontinuous permafrost, and seasonally frozen ground zone over the Xidatan from 1970 to 2019.

Table 4. Variations of the permafrost boundary and areal extent of frozen ground type over the Xidatan for 1970, 2019, and that of projected variations by 2100 under different climate change scenarios.

设置了格式: 字体颜色: 文字 1, 英语(美国)

	The lower limit or the lowest elevation (m a.s.l.)		Areal extent (%)		
	North–facing	South–facing	Con.	Disc.	Seas.
1970	4525(4138)	4732 (4357)	33.93	46.07	20.00
2019	4525 (4185)	4732 (4357)	33.93	33.21	32.86
SSP1–2.6 (2100)	4567 (4308)	4732 (4516)	28.57	30.36	41.07
SSP2–4.5 (2100)	4567 (4308)	4732 (4516)	28.57	28.57	42.86
SSP5–8.5 (2100)	4567 (4309)	4754 (4570)	27.14	21.79	51.07
RCP2.6 (2100)	4567 (4308)	4732 (4416)	28.57	30.36	41.07
RCP4.5 (2100)	4567 (4308)	4732 (4516)	29.29	27.50	43.21
RCP8.5 (2100)	4567 (4309)	4737 (4558)	28.93	22.50	48.57

Note: Outside brackets were the lower limit of the continuous permafrost zone, while in brackets were the lowest elevation of the permafrost boundary. Con., Disc., and Seas. means continuous permafrost, discontinuous permafrost, and seasonally frozen ground, respectively.

设置了格式: 字体颜色: 文字 1

~~**Table 4. The lower limit of continuous permafrost zone and the lowest elevation of permafrost boundary (in brackets) for north- and south- facing slope over the Xidatan for 1970, 2019, and that of projected changes by 2100 under different climate change scenarios (unit: m a.s.l).**~~

~~Orientation~~	~~1970~~	~~2019~~	~~SSP1–26~~	~~SSP2–45~~	~~SSP5–85~~	~~RCP2.6~~	~~RCP4.5~~	~~RCP8.5~~
~~North–facing~~	~~4525 (4138)~~	~~4525 (4185)~~	~~4567 (4308)~~	~~4567 (4308)~~	~~4567 (4309)~~	~~4567 (4308)~~	~~4567 (4308)~~	~~4567 (4309)~~
~~South–facing~~	~~4732 (4357)~~	~~4732 (4357)~~	~~4732 (4516)~~	~~4732 (4516)~~	~~4754 (4570)~~	~~4732 (4416)~~	~~4732 (4516)~~	~~4737 (4558)~~

~~**Table 5. The areal extent percentage of continuous, discontinuous permafrost, and seasonally frozen ground zone over the Xidatan for 1970, 2019, and that of projected variations by 2100 under different climate change**~~

~~scenarios (unit: %).~~

~~Type~~	~~1970~~	~~2019~~	~~SSP1-26~~	~~SSP2-45~~	~~SSP5-85~~	~~RCP2.6~~	~~RCP4.5~~	~~RCP8.5~~
~~Continuous~~	~~33.93~~	~~33.93~~	~~28.57~~	~~28.57~~	~~27.14~~	~~28.57~~	~~29.29~~	~~28.93~~
~~Discontinuous~~	~~46.07~~	~~33.21~~	~~30.36~~	~~28.57~~	~~21.79~~	~~30.36~~	~~27.50~~	~~22.50~~
~~Seasonally~~	~~20.00~~	~~32.86~~	~~41.07~~	~~42.86~~	~~51.07~~	~~41.07~~	~~43.21~~	~~48.57~~

As for permafrost characteristics, regional–average MAGT has increased by 0.44 ℃ over the past 50 years. ~~Along with temperature~~ With temperature warming, we found a gradual decline with a mean amplitude of 0.36 m in the position of the permafrost table whereas a drastic ~~moved~~ moved-up permafrost base of 1.12 m. Correspondingly, permafrost had thawed an average of nearly 1.54 m in thickness ~~an average of nearly 1.54 m in thick of permafrost had thawed~~. Spatially, the mean MAGT warmed ~~by~~ up to 0.49 ℃, and the average permafrost table declined by 0.37 m for the continuous permafrost zone~~, but~~. Still its permafrost base (around -0.80 m) and thickness (around -1.18 m) vary comparatively ~~minor~~. By comparison, comparatively low variations in MAGT (0.40 ℃) and ~~in~~ permafrost table (average declined by 0.76 m), but dramatic changes ~~of an average~~ of -4.23 m occurred in the discontinuous permafrost zone, which is roughly doubled compared to changes on the continuous permafrost area. Correspondingly, an average of about -1.96 m in thick permafrost had quickly thawed, owing to a remarkably rising effect of the permafrost base. ~~n effect of the permafrost base remarkably rising~~.

Table 6. Changes in characteristics of different frozen ground types over the Xidatan for the period 1970 to 2019, and projected changes by the 2090s, relative to the 2010s, under different climate change scenarios. ~~**Table 6. Changes in permafrost characteristics (MAGT, permafrost table, permafrost base, and permafrost thickness) of continuous (Con.), discontinuous permafrost (Disc.) zone over the Xidatan for the period 1970 to 2019, and projected changes by the 2090s, relative to the 2010s, under different climate change scenarios.**~~

	Types	1970–2019	SSP12–2.6	SSP2–4.5	SSP5–8.5	RCP2.6	RCP4.5	RCP8.5
MAGT (℃)	Con.	0.49	0.73	0.94	1.03	0.65	0.91	1.06
	Disc.	0.40	0.53	0.66	0.96	0.48	0.65	0.86
Permafrost table (m)	Con.	0.37	0.56	1.76	6.24	0.44	1.23	4.95
	Disc.	0.35	0.87	3.13	7.02	0.64	2.26	6.13

Permafrost base (m)	Con.	-0.80	-3.52	-3.87	-3.99	-3.41	-3.81	-4.13
	Disc.	-1.60	-4.87	-5.09	-5.17	-4.80	-5.08	-5.17
Permafrost thickness (m)	Con.	-1.18	-4.11	-5.23	-10.38	-3.87	-5.11	-9.42
	Disc.	-1.96	-5.78	-7.94	-12.76	-5.46	-7.44	-11.65

Note: Con., Disc., and Seas. means continuous permafrost, discontinuous permafrost, and seasonally frozen ground, respectively.

设置了格式: 字体: (中文) +中文正文 (等线), 非加粗, 英语 (美国)

带格式的: 段落间距段前: 12 磅, 行距: 1.5 倍行距

3.3. Projection of permafrost condition

The projected changes in the lower limit of the continuous permafrost zone, the lowest elevation of permafrost boundary, and the spatial distribution of continuous, discontinuous permafrost, and seasonally frozen ground as well as its characteristics (MAGT, permafrost table, permafrost base, and permafrost thickness), are presented in Table 4–6 and Fig.10.

The result indicated that the lower limit of continuous permafrost zone on north–facing slopes is projected to increase by 42 m until 2100, relative to 2019, under all RCPs or SSPs~~,~~. On the south-facing slopes, this value is about ~~while, by~~ 22 m ~~on south–facing slopes~~ under very high emission scenarios (SSP5–8.5 or RCP8.5), which is far smaller than the changes in the lowest elevation of the permafrost boundary. The lowest elevation of permafrost boundary on the north–facing slopes is projected to increase by 123 m by 2100, relative to 2019, under both low and medium emission scenarios, and by 124 m under very high emission scenarios SSP5–8.5 or RCP8.5. South-facing slopes are ~~As for south–facing slopes, it is~~ projected to increase by 159 m by 2100, compared to 2019, under both low and medium emission of RCP or SSP scenarios~~,~~. ~~but~~ Still a more pronounced increase of around 213 and 201 ~~m,~~ m, is ~~respectively, are~~ projected under SSP5-8.5 and RCP8.5. Relative to 2019, the areal extent of continuous permafrost zone is projected to decrease by 5.36 (5.36), 5.36 (4.64), and 6.79 (5.00) %, respectively, by 2100, under SSP1–2.6 (RCP2.6), SSP2–4.5 (RCP4.5), and SSP5–8.5 (RCP8.5). Compared with the decrease of 3.57 (2.85), 4.64 (5.71), and 11.42 (10.71) % for discontinuous permafrost zone. ~~By~~ In contrast, the areal extent of seasonally frozen ground is projected to increase by 8.93 (8.21), 10.00 (10.36), and 18.21 (15.71) %, respectively, by 2100, relative to 2019, under SSP1–2.6 (RCP2.6), SSP2–4.5 (RCP4.5), and SSP5–8.5 (RCP8.5). The northern limit of the continuous permafrost zone is projected to retreat

southwards around 1~2 km under SSP1–2.6 (RCP2.6) or SSP2–4.5 (RCP4.5) or RCP8.5, and about 1~3 km under SSP5–8.5. By comparison, the northern boundary of the discontinuous permafrost zone is anticipated to shift southward around 1 km under SSP1–2.6 (RCP2.6) or SSP2–4.5 (RCP4.5), and around 1~2 km under SSP5–8.5 (RCP8.5).

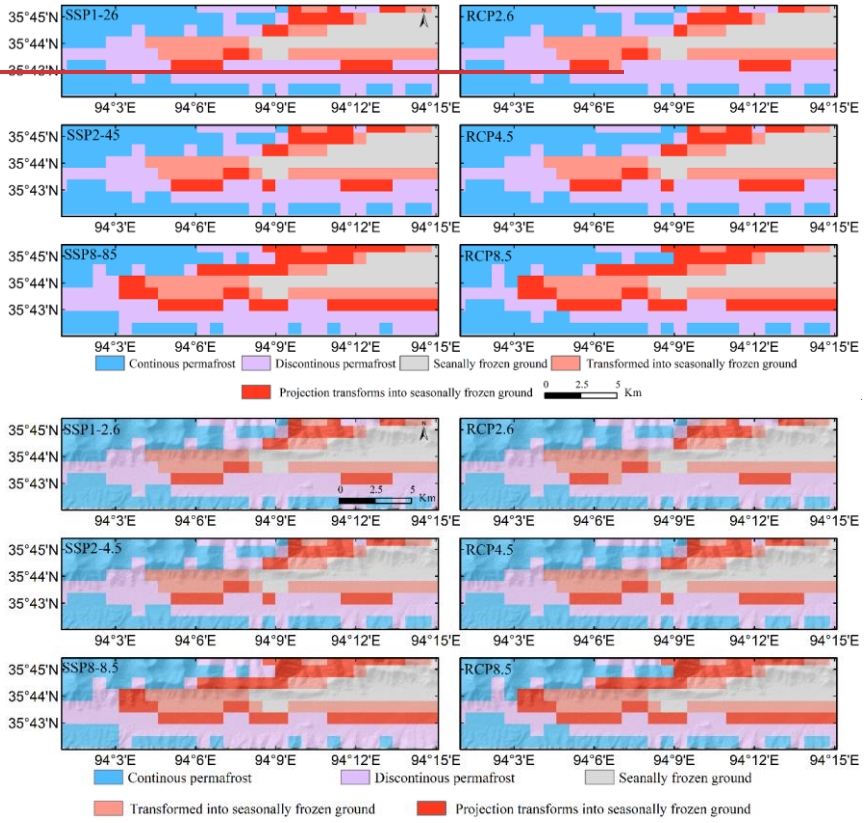

Figure 10. Projected spatial distributive changes of different frozen ground types ~~continuous, discontinuous, and seasonally frozen ground~~ over the Xidatan in the future period by 2100 under RCPs and SSPs scenarios (left column, from top to bottom, each row shows under SSP1–2.6, SSP2–4.5, and SSP5–8.5 scenarios, right column, from top to bottom, each row shows under RCP2.6, RCP4.5, and RCP8.5 scenarios).

Under global climate ~~gradual~~ warming ~~climate~~ scenarios, the permafrost temperature is anticipated to increase further ~~increase~~, but its variation lags substantially behind the changes in air temperature. The regional–average MAGT is projected to ~~further~~ warm by 0.63, 0.81, and

0.99 ℃, respectively, by ~~the~~ 2090s, relative to ~~the~~ 2010s, under SSP1–2.6, SSP2–4.5, SSP5–8.5, which is ~~slighter~~ slightly higher than that of RCP scenarios (0.56, 0.78, and 0.98 ℃, respectively). Along with MAGT rising, relative to the 2010s, the permafrost table is projected to further decline by 0.72 to 6.70 m under SSP scenarios (0.72 m, 2.48 m, and 6.70 m, respectively, under SSP1–2.6, SSP2–4.5, and SSP5–8.5), and decline by 0.54 to 5.47 m under RCP scenarios (0.54 m, 1.73 m, and 5.47 m, respectively, under RCP2.6, RCP4.5, and RCP8.5), at the end–century (the 2090s). The average permafrost base is projected to rise by 4.22, 4.54, and 4.56 m, respectively, by the 2090s, compared to the 2010s, under SSP1–2.6, SSP2–4.5, and SSP5–8.5. Meanwhile, a relative decrease in permafrost base of 4.14, 4.43, and 4.60 m, ~~respectively,~~ are estimated under RCP2.6, RCP4.5, and RCP8.5. An average thinning in the permafrost thickness is projected to be 4.97, 6.66, and 11.74 m, respectively, under SSP1–2.6, SSP2–4.5, and SSP5–8.5, and that would be 4.71, 6.26, and 10.43 m, respectively, under RCP2.6, RCP4.5, and RCP8.5.

Spatially, the average MAGT is projected to rise by 0.73 (0.65), 0.94 (0.91), and 1.03 (1.06) ℃, respectively, for continuous permafrost zone, under SSP1–2.6 (RCP2.6), SSP2–4.5 (RCP4.5), and SSP5–8.5 (RCP8.5). Compared with the rising of 0.53 (0.48), 0.66 (0.65), and 0.96 (0.86) ℃, respectively, for discontinuous permafrost zone. As for the permafrost table, both continuous and discontinuous permafrost zone ~~are~~ is projected to gradual decline under SSP1–2.6 (0.56 and 0.87 m), and RCP2.6 (0.44 and 0.64 m), but a remarkable decline are ~~is~~ projected under medium ~~and very~~. Very high emission scenarios, and a more pronounced decline is anticipated under SSPs scenarios than that projection under RCPs scenarios. The average permafrost table in continuous permafrost zone is projected to decline by 1.76 (1.23) and 6.24 (4.95) m, respectively, under SSP2–4.5 (RCP4.5) and SSP5–8.5 (RCP8.5). Compared with the decline of 3.13 (2.26) and 7.02 (6.13) m, respectively, under SSP2–4.5 (RCP4.5), and SSP5–8.5 (RCP8.5) for continuous permafrost zone. Permafrost base is projected to ~~remarkably~~ move remarkably up under all scenarios. For continuous permafrost zone, permafrost base is projected to rise by 3.52 (3.41), 3.87 (3.81), and 4.13 (3.99) m, respectively, under SSP1–2.6 (RCP2.6), SSP2–4.5 (RCP4.5), and SSP5–8.5 (RCP8.5), which is slightly smaller than that projected for discontinuous permafrost zone (4.87 (4.80), 5.09 (5.08), and 5.17 (5.17) m, respectively, under SSP1–2.6 (RCP2.6), SSP2–4.5 (RCP4.5), and SSP5–8.5 (RCP8.5)). The average permafrost thickness of continuous and discontinuous

permafrost zone is projected to thin~~ning~~ 4.11 (3.87) and 5.78 (5.46) m, respectively, under SSP1–2.6 (RCP2.6) as the main effect of permafrost base move up. Whereas a more prominent decrease of 5.23 (5.11) and 7.94 (7.44) m, respectively, under SSP2–4.5 (RCP4.5), 10.38 (12.76), and 9.42 (11.65) m, respectively, under SSP5–8.5 (RCP8.5), owing to both effect of permafrost table declining and the permafrost base rising.

4 Discussion

4.1 Comparison with previous studies

In this work, our simulated distribution of continuous permafrost zone had a substantial agreement with three permafrost maps investigated in 1975, 2012, and 2016~~,~~. ~~but~~ Still a remarkable difference in the discontinuous permafrost zone where permafrost and seasonally frozen ground coexist (Fig. 6). Compared with the 2016 map and our simulated results, the 1975 and 2012 maps underestimated the permafrost area in the discontinuous permafrost zone. This contradiction might be due to differences using data, methods, study periods, spatial resolutions, etc. (Yang et al., 2010; Ran et al., 2012; Zou et al., 2017). The 1975 and 2012 maps were plotted on a topographic map at a 1:50000 scale based on field ~~data~~investigations, aerial photographs, and satellite images (Nan et al., 2003; Luo et al., 2018). These ~~coarse~~ coarse-resolution maps can't accurately consider the effect of local factors since they cannot describe variations ~~of~~ in ground conditions over a short distance (Zhang et al., 2013). Moreover, comparing them with field observations makes the result difficult to validate. ~~the result is difficult to validate by comparing them with field observations~~. Although the 1975 and 2012 maps may represent the corresponding permafrost situations in that year, they are limited by field investigations, and there is not a clear understanding of whether permafrost existed in the northeaster high-altitude areas or not. In the 2012 map, ~~and~~ these isolated top mountain areas are uniformly considered as the seasonally frozen ground when permafrost mapping (Luo et al., 2018), which is unreasonable and underestimated in the areal coverage of the permafrost in that area. Furthermore, the artefactual errors were hard to control when mapping permafrost distribution by conventional cartographic techniques that delineated the permafrost boundaries on the topographic maps ~~by hand~~manually (Zou et al., 2017; Ran et al., 2012). These factors inevitably led to existing uncertainties in the 1975 and 2012 maps.

By comparison, the 2016 map and our simulation results have a much higher spatial resolution (1 km×1 km) than ~~field~~ field-investigated–based ones (e.g., 1975 and 2012 maps) by improved MODIS LST ~~data~~ application. In addition, it showed higher and more accuracy in identifying both permafrost and seasonally frozen ground boreholes and performed better at recognizing the seasonally frozen ground in regions with complex terrain. This finding highlights the potential advantage of remote sensing–based data in improving the spatial modeling of margin~~s~~al permafrost simulations on the QTP. Overall, our simulated distribution of continuous permafrost and discontinuous permafrost zone was similar to that of the 2016 map. Differences mainly the TTOP model did not consider the thermal state of the deep permafrost. Therefore, the areal extent of permafrost distribution in the 2016 map likely was slightly underestimated compared with our simulation results. Moreover, the 2016 map assumes that permafrost is in equilibrium with the long-time climate. However, the ground temperature observations of permafrost on the QTP have increased during the past several decades (Zou et al., 2017; Zhao et al., 2010, 2020; Yao et al., 2019; Ehlers et al., 2022), and this means a disequilibrium of permafrost under ongoing climate warming. So, map based on a contemporary climate forcing is likely to underestimate the extent of permafrost (Zou et al., 2017). By contrast, in our study, we used a transient numerical heat conduction permafrost model, which integrated climate and ground condition variables to quantify the change in permafrost. Our model performed well in modeling the disappeared evolution of two permafrost islands since 1975, and shifting the northern boundary of discontinuous permafrost (Fig. 6d–f), which can be confirmed by direct observation ~~observed boreholes~~ (Jin et al., 2006; Luo et al., 2018; Yin et al., 2021). These phenomena implied our model could accurately capture marginal permafrost thermal state dynamics ~~dynamics of marginal permafrost thermal state~~ under a warming climate.

Furthermore, using our model, we quantified the spatial distribution of permafrost over the study area. We simulated a striking elevation dependence in permafrost distribution. Specifically, permafrost temperature decreases, decreases in thickness and~~permafrost thickness thicker, and~~ the permafrost table becomes thinner with the elevation increase, which are consistent with previous observed–based studies (Cheng et al., 1984; Wu et al., 2010; Zhao et al., 2010, 2019, 2020; Li et al., 2012; Jin et al., 2011; Luo et al., 2018). Moreover, Cheng et al. (2019) indicated the MAGT varied from -5 to 0.5℃, and the average permafrost thickness was approximately 26 m here, as deduced

by considerable monitoring and field investigation dataset. ~~Furthermore,~~And the monitoring network of ALT along the Qinghai–Tibet Highway (QTH) by Li et al. (2012) has demonstrated that the mean ALT was 218 cm, ~~with a range~~ ranging from 100 to 320 cm from 1981 to 2010.

This evidence strongly corroborates our simulation results accuracy, giving us more confidence in upscaling our model to the study area to investigate spatiotemporal dynamics and anticipate possible changes in permafrost. ~~These pieces of evidence are strongly corroborating the accuracy of our simulation results, which gives us more confidence in upscaling our model to the whole study area to investigate spatiotemporal dynamics and anticipate possible future changes in permafrost.~~

4.2 Process of permafrost degradation

In this paper, we simulated a slow response of the permafrost thermal state to a warming climate in the northern lower limit of the permafrost zone (Xidatan) on the QTP. As shown in our simulation, from 1970 to 2019, we simulated that roughly 12.86 % of the discontinuous permafrost zone over the study area has ultimately converted into ~~the~~ seasonally frozen ground, which is very close to observed facts~~a field investigation of permafrost changes~~ (13.8 %) here in 2012 (Luo et al., 2018). Permafrost distribution and its thermal conditions over the study area were spatially ~~Spatially, permafrost distribution and its thermal conditions over the study area were~~ controlled by elevational. In addition, due to the orientation of slopes influences the amount of solar radiation received by the ground surface (Cheng et al., 2004). Much thicker, colder permafrost and a thinner ALT on north-facing slopes than on south-facing slopes within the same elevation. So, a distinct spatial discrepancy of permafrost thermal regimes in response to a warming climate. Over the past 50 years, the rising rate of MAGT for the continuous permafrost zone was relatively faster (regional–average warmed by 0.49 ℃) due to more energy being available to heat the ground. By contrast, as permafrost temperature is close to the thawing point (about 0 ℃), accumulated energy is enormously consumed by melting ground ice, and MAGT for the discontinuous permafrost zone slowly rises (regional–average warmed by 0.40 ℃). Meanwhile, both the continuous (regional–average declined by 0.37 m) and discontinuous permafrost zone (regional–average declined by 0.35 m) displayed a gradual decline in the position of the permafrost table. But we simulated a drastically risen permafrost base, especially in the discontinuous permafrost zone, ~~which is~~ due to heat transfer in

strata from top to bottom leading the geothermal gradients in permafrost to keep dropping. When the geothermal gradient in permafrost temperature drops to less than that of the underlying thawed soil layers, the geothermal heat flux from the deep stratum is completely used to thaw the permafrost base. So, permafrost thaws from bottom to top and moves upward. As permafrost was relatively warm and thin and geothermal flow relatively high over the Xidatan (Wu et al., 2010, Sun et al., 2019), the degradation mode of permafrost over this region is simulated to be upward thawing from the permafrost base. This degradation mode is also confirmed by several monitoring boreholes across this region (Jin et al., 2006, 2011; Cheng and Wu. 2007; Liu et al., 2020). In general, the pattern of permafrost degradation over the Xidatan from 1970 to 2019 can be summarized like this: the continuous permafrost zone has gradually converted to warm permafrost, whereas the discontinuous permafrost zone has been upward thawing remarkably. Notably, the ~~edge areas~~margin of the discontinuous permafrost zone have converted to seasonally frozen ground.

As for the projections under different climate change scenarios, the latest generation of GCMs from CMIP6 projected a substantially warmer climate by 2100 than the previous generation, for instance, CMIP5 (Fewster et al., 2022). In our study, MAGT is anticipated further increase, and the warm rate is projected to be slighter higher under SSP than ~~that of~~ RCP, but very small discrepancies among SSP and RCP scenarios in projected changes of permafrost distribution extent. This further verified the response of permafrost to climate warming is a slow and nonlinear process, and its variation lags substantially behind the changes in air temperature. But contrary findings are reported by some previous studies. Based on the empirical equilibrium model, Lu et al. (2017) predicted that extensive reduction of permafrost area on the QTP by the end of the 21st century under RCP2.6 (22.44 %) and RCP8.5 (64.31 %), and permafrost would retreat into the Qiangtang Plateau hinterland. Likewise, Chang et al. (2018) suggested that the permafrost area on the QTP is projected to shrink by 9.7 %, and 10.7 %, under RCP4.5 and RCP8.5, respectively, in the next 20 years, and that is projected to by 26.6 % and 32.7 %, respectively, in the next 50 years. ~~Based on the surface frost index model,~~ Guo and Wang (2016) projected almost no permafrost on the QTP by 2080 to 2099 under RCP8.5. In addition, Yin et al. (2021) projected around 26.9 %, 59.9 %, and 80.1 % of permafrost on the QTP is likely to disappear~~, respectively~~, by the end of the 21st century under SSP1–2.6, SSP2–4.5, and SSP5–8.5 scenarios. For numerical modeling, Guo et al. (2012) applied

the Community Land Model4 (CLM4) to project an approximately 81% reduction in near-surface (<4.5 m) permafrost area on the QTP by the end of the 21st century under the A1B emission scenario. Additionally, the deep permafrost depths of 10 and 30 m would be largely degraded by the year 2030-2050. Zhang et al. (2022) applied Noah LSM to project much of 44 ± 4%, 59 ± 5%, and 71 ± 7% permafrost is likely to degrade in the late 21st century, under SSP2-4.5, SSP3-7.0, and SSP5-8.5 scenarios, respectively.

The abovementioned results and our projections unanimously projected that further degradation trend in permafrost on the QTP under warming climate scenarios, but a considerable discrepancy among results on the magnitude of permafrost degradation. This discrepancy can partly be attributed to those approaches that attributed to those approaches established a simple statistical relationship between the current permafrost distribution and air temperature based on the surface energy balance theory. However, permafrost in the QTP formed over a long period of cold paleoclimate and developed an energy state characterized by low ground temperature and ground ice in permafrost (Sun et al., 2019; Zhao et al., 2020; Jin et al., 2011). The present state of permafrost is a response to historical climate changes and impacts future development (Wu et al., 2010; Cao et al., 2014). However, the current project of permafrost degradation does not consider the historical energy accumulation in permafrost and the impact of ground ice conditions buried below 1 m underground (Zhao et al., 2020; Smith et al., 2022). For example, most of LSMs studies mainly focused on optimizing parametrization schemes for shallow soil layer (<4 m) and simply extending the soil column simulation depth, whereas it was poor considering the effecting of thermal state of deep permafrost and effecting of ground ice existence (Lee at al., 2014; Sun et al., 2019). Furthermore, ignoring the geothermal heat flux by setting zero flux or constant temperature as the bottom boundary condition (Wu et al., 2010; Xiao et al., 2013). However, these factors play a crucial role in the long-term evolution of permafrost in general (Zhao et al.,2020). Thus, the relationship between the decrease in the areal extent of permafrost and the warming air temperature over the present-day permafrost region is approximately linear simulated by these empirical statistics or LSMs. Given that such high rates of permafrost loss are not observed, and this indicates a too-high sensitivity for those models predicting such losses (Zhao et al., 2020).

~~The abovementioned results were modeling of permafrost degradation by the statistical relationship between the current permafrost distribution and air temperature, based on the surface energy balance theory together with heat conduction theory. However, permafrost in the QTP formed over a long period of cold paleoclimate and developed an energy state characterized by low ground temperature and ground ice in permafrost (Sun et al., 2019; Zhao et al., 2020; Jin et al., 2011). The present state of permafrost is a response to historical climate changes and impacts future development (Wu et al., 2010; Cao et al., 2014). But, Current models of future permafrost degradation do not consider the historical energy accumulation in permafrost as well as the impact of ground ice conditions buried below 1 m underground (Zhao et al., 2020; Smith et al., 2022).~~

~~Therefore, the projection of the response of the permafrost degradation in climatic warming deduced by the method abovementioned shows a nearly linear with time under a warming climate and consequence more severe permafrost thawing, especially in the deep permafrost compared with our simulations. In comparison, the magnitude and evolution of permafrost degradation projections on the QTP derived from our transient simulations agree well with that of the heat conduction permafrost model account for the thermal state of deep ground ice (Li et al., 1996; Li et al., 2008; Sun et al., 2019). Both these simulations and our modeling can well describe the heat transfer process in permafrost and reasonably capture the attenuation and time lag of heat transfer in deep permafrost as water or ice content and ground is a poor conductor of heat. It can be noted that existing studies largely ignore the thermal properties of deeper permafrost, but our findings highlight initial permafrost thermal state is influenced by historical climate, stratigraphic thermal properties, ground ice distribution, geothermal heat flow, and propagation of the phase transition interface plays a critical role in permafrost degradation.~~

~~-~~In comparison, our model considers the thermal properties difference between frozen and thawed soil, the phase variations of the unfrozen water in frozen soil, the distribution of the ground ice, and geothermal heat flow. Thereby, well describe the heat transfer process in permafrost and reasonably capture the attenuation and time lag of heat transfer in deep permafrost as water or ice content and ground is a poor conductor of heat. Moreover, our model is characterized by vertical modeling domains of one hundred meters with a vertical resolution of 0.05 m within the active layer

(the upper 4 m) and provides sufficient accuracy to resolve the annual dynamics of active layer thawing and refreezing, as well as the evolution of ground temperatures in deeper layers. Our simulation results in compliance with the observed facts. The magnitude and evolution of permafrost degradation projections on the QTP derived from our transient simulations were agree well with that of the heat conduction permafrost model account for the thermal state of deep ground ice (Li et al., 1996; Li et al., 2008; Sun et al., 2019). It can be noted that existing studies largely ignore the thermal properties of deeper permafrost, but our findings highlight initial permafrost thermal state is influenced by historical climate, stratigraphic thermal properties, ground ice distribution, geothermal heat flow, and propagation of the phase–transition interface plays a critical role in permafrost degradation.

4.3 Model uncertainties

~~In this study, the numerical simulations by our transient permafrost model may have uncertainties, including the extended MODIS LST series used as the model inputs, the parameters of the soil, and the physics of the permafrost model. Due to a significant linear relationship between LST and AT over the study area, moreover, in this work, we mainly focus on the long–trend permafrost temperature over the foreseeable future. The biases of the estimated LST by simple regression relationship of AT–LST cannot affect the long–term mean change trend in LST. Furthermore, although field and modeling studies suggest that heat transfer is a good approximation for most permafrost areas (Weismüller et al., 2011), other physical processes of energy transfer (e.g., convective, lateral) do occur and may play a vital role in transforming from stable to degrading permafrost (Jin et al., 2006, 2011; Kane et al., 2001; Westermann et al., 2016). In our study, heat conduction is considered the principal means of energy transfer on the ground. Hence, we simulated may conservatively change in the soil temperature, which can be improved by taking other physical processes of heat transfer into consideration in future studies.~~

In this study, there are may have uncertainties, including the extended MODIS LST series used as the model inputs, soil parameters heterogeneity at sub-grid in terms of surface cover, topography, and soil stratigraphy, and the physics of the permafrost model. Due to a significant linear relationship between LST and AT over the study area, moreover, in this work, we mainly focus on the long–trend permafrost temperature over the foreseeable future. The biases of the estimated LST by simple

regression relationship of AT–LST cannot affect the long–term mean change trend in LST. Furthermore, the limitation of the current model is one-dimensional, which assumes each grid cell to be uniform without lateral exchange. Our simulations, therefore, are considered as conservatively changes in the ground temperature in areas with lateral water fluxes, such as flood land in the valley. The representation of the horizontal fluxes exchange of heat and water deserves increased attention in future modeling approaches, and coupling the current model with this physical process of heat transfer could be an important step toward better simulation results of high-resolution in the next generation of permafrost models. Moreover, we projected the possible fate of permafrost over Xidatan by 2100, under an area-mean warming rate scenario of QTP. Hence, the anticipated permafrost degradation in this study, may not be the actual overview, as it does not consider the regional-level or small-scale-based future climate change. However, we believe that our simulation results can provide a relatively reasonable projection of marginal permafrost degradation magnitude on the QTP under the different climate change scenarios in the foreseeable future. Meanwhile, high-resolution climate models and improved numerical representations of atmospheric circulation systems and land-atmosphere interactions over the heterogeneous QTP region could be crucial in improving the GCMs/RCMs performance, which improve the accuracy in the projection of permafrost degradation in the future.

5 Conclusions

This study applied a new transient numerical permafrost model for modeling permafrost distribution and its thermal dynamics at 1 km×1 km resolutions near the northern limit of permafrost on the QTP for current (1970–2019) and future (2020–2100). Overall, we simulated vertical ground temperature profiles and ALT closely matching with the long-term continuous field observations over the study area. This ~~match with the long-term continuous field observations over the study area, which~~ means our model can well-describe the heat transfer process in permafrost and reasonably capture heat attenuation and time lag ~~the attenuation and time lag of heat~~ in deep permafrost. Furthermore, we accurately identified permafrost boundaries, and can realistically capture the evolution of the permafrost thermal regime. According to the simulations, ~~we found~~ permafrost distribution and its thermal conditions over the study area were controlled by elevational with a

strong influence of slope aspects. From 1970 to 2019, the lowest elevation of permafrost (north–facing slope aspect) rose approximately 47 m, and the northern boundary of discontinuous permafrost retreated southwards approximately 1~2 km. But that remains unchanged for the continuous permafrost area. Meanwhile, the regional average MAGT has warmed by 0.44 °C~~, and by~~and 0.49 °C, respectively, on continuous and discontinuous permafrost zone. In general, over the past 50 years, the continuous permafrost zone over the study area has gradually converted to warm permafrost, whereas the discontinuous permafrost zone has been upward thawing remarkably, and the~~-~~ margin of the ~~edge areas of~~ the discontinuous permafrost zone are reduced by about 12.86%. Under gradual warming climate scenarios, the MAGT is anticipated to rise further ~~further rise~~ in the future, and the warm rate is projected to be slighter higher under SSP than RCP. However, there are no distinct discrepancies in projection changes in the areal extent of permafrost among SSP and RCP scenarios. These findings highlight the slow process and delays in the response of mountain permafrost to a warming climate, and our projected change rate in the permafrost extent is far less than some simulation results that do not account for the effects of water phase change, historical climate change, and the thermal state of deep permafrost. In summary, our study provides improved simulations for permafrost distribution and thermal regime dynamics in marginal permafrost on the QTP at decadal to centennial time scales. More importantly, these results may give a better understanding of degradation processes and mechanisms of marginal permafrost on the QTP, and guidelines for the further accurate evaluation of changes in the areal extent of the permafrost on the QTP hinterland.

Appendix A

Table A1. A list of monitoring boreholes in the study area and a summary of the ground properties are shown.

Borehole (altitude/ m a.s.l.)	Coordinates	Sensor depths (m)	Frozen ground type	Soil stratigraphy
QT09 (4538)	35°43′02″ 94°07′05″	0.5–5 m (0.5 m intervals) 5–20 m (1 m intervals) 20–30 m (2 m intervals)	Permafrost	Loam (0–0.2 m) Sandy loam (0.2–1.4 m) Sandy loam with gravel (1.4–2.4 m) Sandy with gravel (2.4–10 m) Rock (10–21 m)
TB01 (4530)	35°43′00″ 94°04′09″	Same as QT09	Permafrost	Sandy loam (0–1.2 m) Sand (1.3–3 m)

				Sand with gravel (3–10 m) Weathered mudstone (>10 m)
XD1–1 (4379)	35°41′55″ 94°12′05″	0.5–10 m (0.5 m intervals) 10–15 m (1 m intervals)	Permafrost	Sandy cobble (0–4.5 m) Fluvial sand (4.5–15 m)
XD1–2 (4377)	35°41′59″ 94°12′07″	Same as XD1–1	Permafrost	Sandy cobble (0–4.5 m) Fluvial sand (4.5–15 m)
XD1–3 (4576)	35°42′04″ 94°12′07″	Same as XD1–1	Permafrost	Sandy cobble (0–5 m) Fluvial sand (5–15 m)
XD1–4 (4374)	35°42′10″ 94°12′07″	Same as XD1–1	Permafrost	Sandy cobble (0–5.5 m) Fluvial sand (5.5–15 m)
XD1–5 (4370)	35°42′16″ 94°12′08″	0.5–8 m (0.5 m intervals)	Permafrost	Sandy cobble (0–5.5 m) Fluvial sand (5.5–10 m)
XD1–6 (4368)	35°42′24″ 94°12′09″	Same as XD1–5	Seasonally frozen ground	Sandy cobble (0–4.5 m) Fluvial sand (4.5–8 m)
XD2–1 (4508)	35°41′56″ 94°05′08″	Same as XD1–1	Permafrost	Sand (0–2.5 m) Sand with massive ground ice (2.5–7 m) Clay (7–9 m) Weathered mudstone (9–15 m)
XD2–2 (4503)	35°42′01″ 94°05′09″	Same as XD1–1	Permafrost	Sand (0–2.8m) Sand with massive ground ice (2.5–6 m) Weathered mudstone (6–15 m)
XD2–3 (4500)	35°42′10″ 94°05′09″	Same as XD1–1	Permafrost	Sand cobble (0–4 m) Fluvial sand (4–15 m)
XD2–4 (4498)	35°42′18″ 94°05′09″	Same as XD1–1	Seasonally frozen ground	Sandy cobble (0–4 m) Fluvial sand (4–15 m)
XD2–5 (4493)	35°42′26″ 94°05′10″	Same as XD1–1	Seasonally frozen ground	Sandy cobble (0–4 m) Fluvial sand (4–15 m)
XD2–6 (4490)	35°42′36″ 94°05′11″	Same as XD1–1	Permafrost	Sandy cobble (0–4 m) Fluvial sand (4–15 m)
XD2–7 (4492)	35°43′00″ 94°05′05″	Same as XD1–5	Seasonally frozen ground	Sand (0–4.5 m) Sandstone (4–8 m)
JXG (4530)	35°43′12″ 94°04′01	1–10 m (1 m intervals) 10–30 m (2 m intervals)	Permafrost	--
CRSQTP (4530)	35°43′ 94°05′	0.4 m 1.6 m 4–10 m (2 m intervals) 10–18 m (4 m intervals) 18–20 m (2 m intervals) 20–29 m (3 m intervals)	Permafrost	--
XD1 (4427)	35°43′12″ 94°08′24″	--	Permafrost	--
XD2 (4530)	35°43′12″ 94°04′14″	--	Permafrost	--
XD3 (4480)	35°43′12″ 94°05′24″	--	Permafrost	--
XD4 (4427)	35°42′00″ 94°08′24″	--	Permafrost	--
XDT1 (4602)	35°42′36″ 94°02′24″	--	Permafrost	--
XDT2 (4530)	35°42′36″ 94°05′24″	--	Permafrost	--
CN13 (4448)	35°42′12″ 94°07′48″	--	Permafrost	--

Note: The symbol--is field-observed frozen ground types collected from previously published literature (Wang et al.,

2000; Jin et al., 2000,2006; Cheng et al., 2007).

Table A2. Calibration thermophysical parameters of different soil layers used for soil temperature modelling.

Texture	*K* (W m^{-1} °C $^{-1}$)		*C* (kJ m^{-3} °C^{-1})		VWC (%)
	Frozen	Thawed	Frozen	Thawed	
Loam	1.25–1.57	0.85–1.28	1639–1879	2208–2475	15–20
Clay	0.83–1.30	0.61–1.03	1756–1907	1881–2191	15–20
Sandy loam	1.31–1.93	1.17–1.71	1844–2107	2258–2634	10–20
Loamy sand	1.02–1.38	1.11–1.24	2040–2208	2541–2676	15–20
Sand cobble	1.0–1.29	0.89–1.10	1639–1739	2007–2208	13–15
Fluvial sand	1.32–1.60	1.09–1.30	1288–1413	1568–1819	6–10
Sand	1.86–2.15	1.48–1.64	1505–1639	1940–2208.1	10–14
Sandstone	0.94–1.91	0.77–1.47	1317–1459	1493–1777	2–6
Sand with Gravel	1.91–2.20	1.47–1.68	1459–1601	1777–2061	6–10
Weathered mudstone	2.27	1.71	1543	1881	6
Rock	0.33	0.33	1940	1940	2

Note: *K* is the thermal conductivity; *C* is the volumetric heat capacity; as well as *VWC* represents total volumetric water/ice content. Soil texture information from Luo et al. (2018) and Liu et al. (2021), the values of thermal conductivity and heat capacity were from Construction of Ministry of PRC. (2011) and Yershov. (2016), and fine–adjusted during the calibration, water content was determined by the soil samples of the borehole cores combined with the observation dataset vicinity of QT09 and the ground ice distribution maps from Zhao et al. (2010).

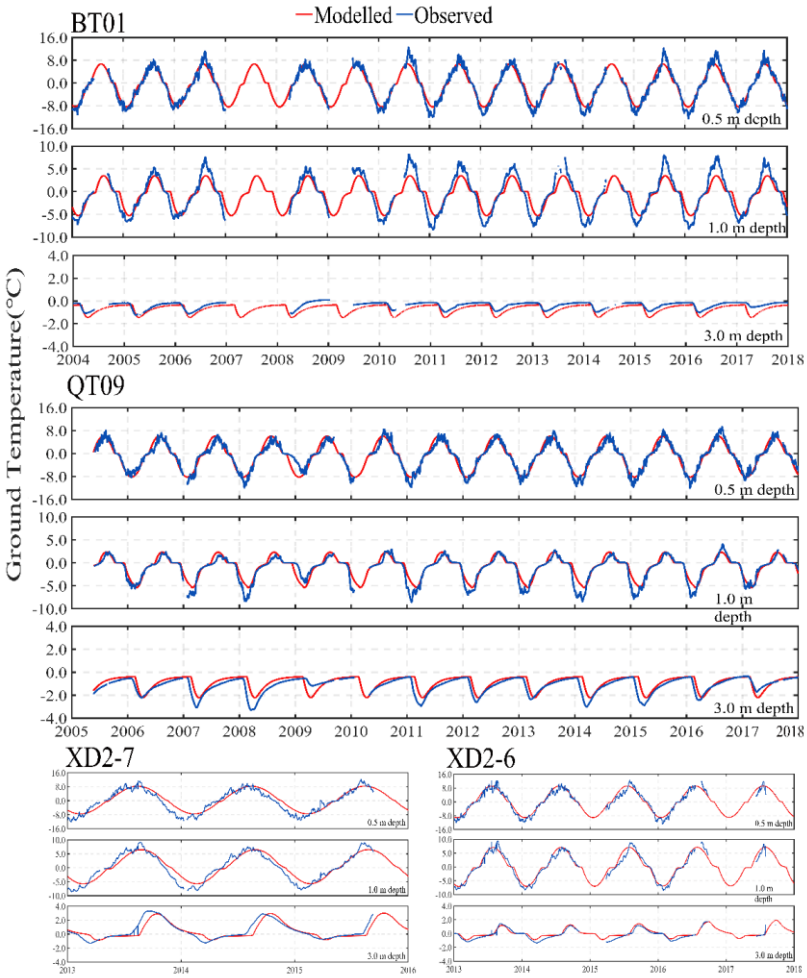

Figure A1. Comparison of the simulated (red lines) to observed (blue lines) daily mean ground temperature at 0.5 m, 1.0 m, 3.0 m depth in four calibration boreholes (BT01, XD2-7, QT09, and XD2-6) during the observation period (There were some data gaps due to temperature probe failure in some years, at the BT01, the data gaps in the record mainly occurred at 0.5-15 m in 2007-2008, and at 15-30 m during the 2005-2007 and 2011-2018, at the QT09, observations at 15-30 m of 2006-2008, 2011-2013, and 2015-2018 are not available, at the XD2-6, the data gap in the record in 2016-2017).

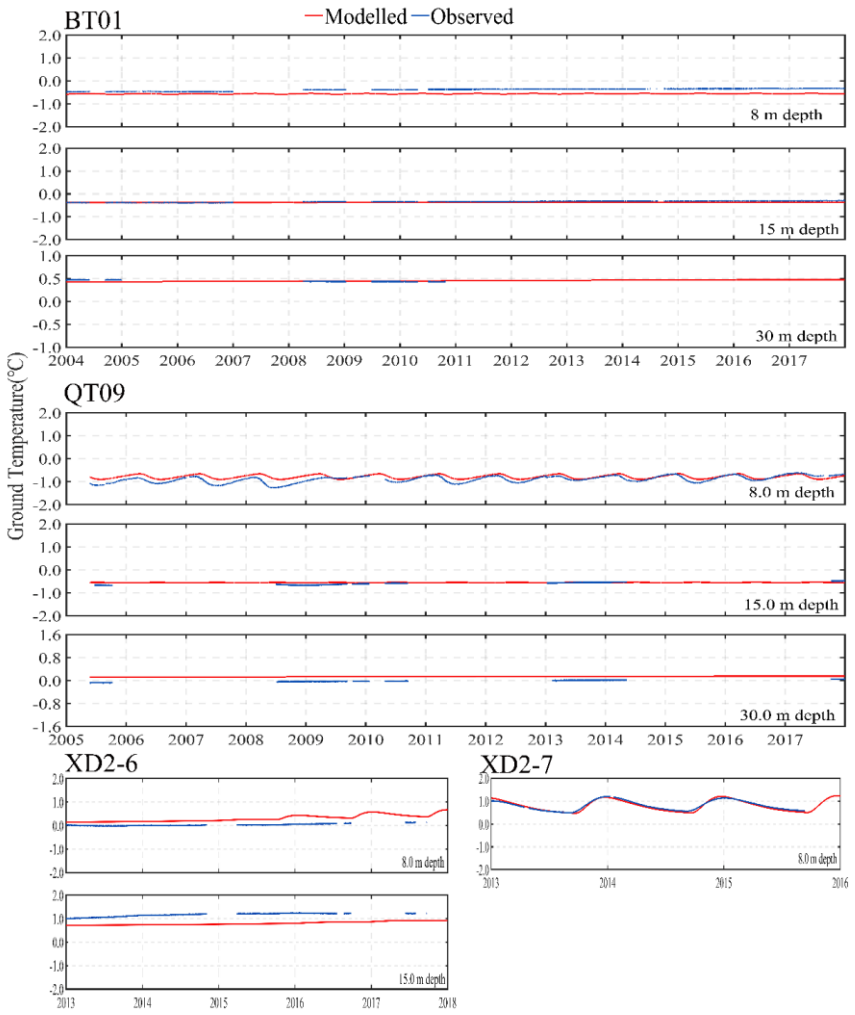

Figure A2. Same as Figure 2. but for daily mean ground temperature at 8 m, 15 m, and 30 m.

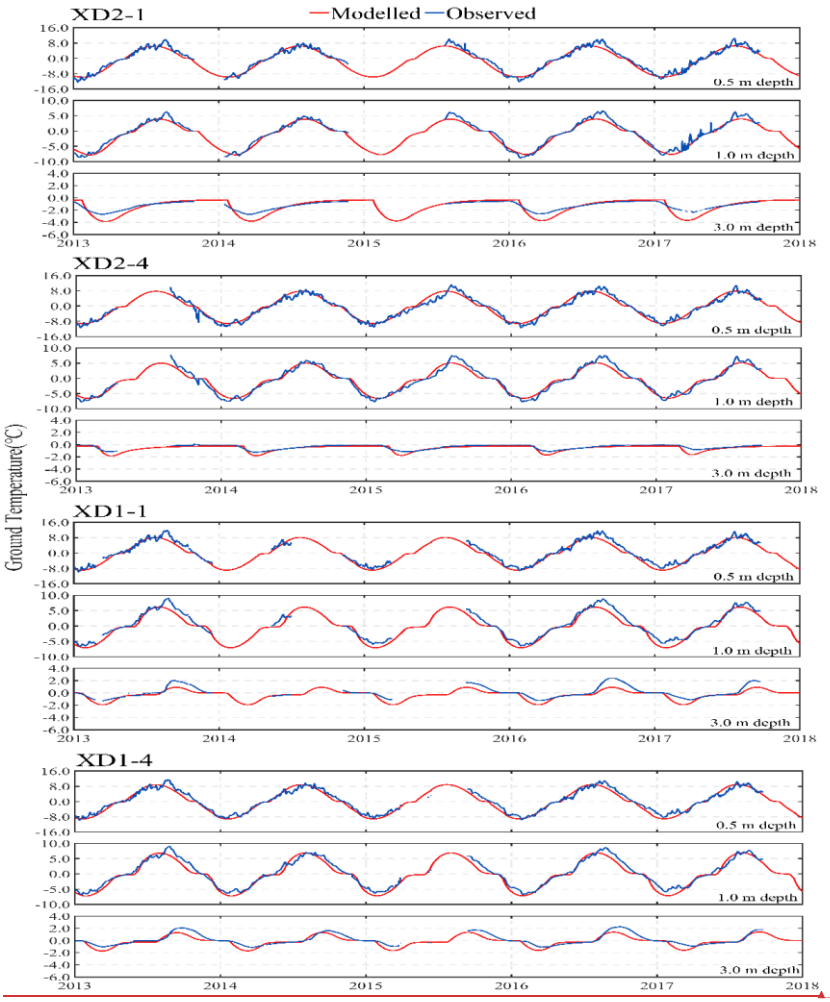

Figure A3. Comparison of the simulated (red lines) to observed (blue lines) daily mean ground temperature at 0.5 m, 1.0 m, and 3.0 m depth in four validation boreholes (XD2-1, XD2-4, XD1-1, and XD1-4) during the observation period from 2013 to 2018 (There were some data gaps due to temperature probe failure in some years, at the XD2-1, the data gaps in the record mainly occurred at 0.5-3.0 m in the first half of 2015, at the XD1-1, the data gap in the record at 0.5-3.0 in 2014-2015, at 8-15 m during the 2013-2015, at the XD1-4, the data gap in the record in the first half of 2015).

设置了格式: 英语(美国)

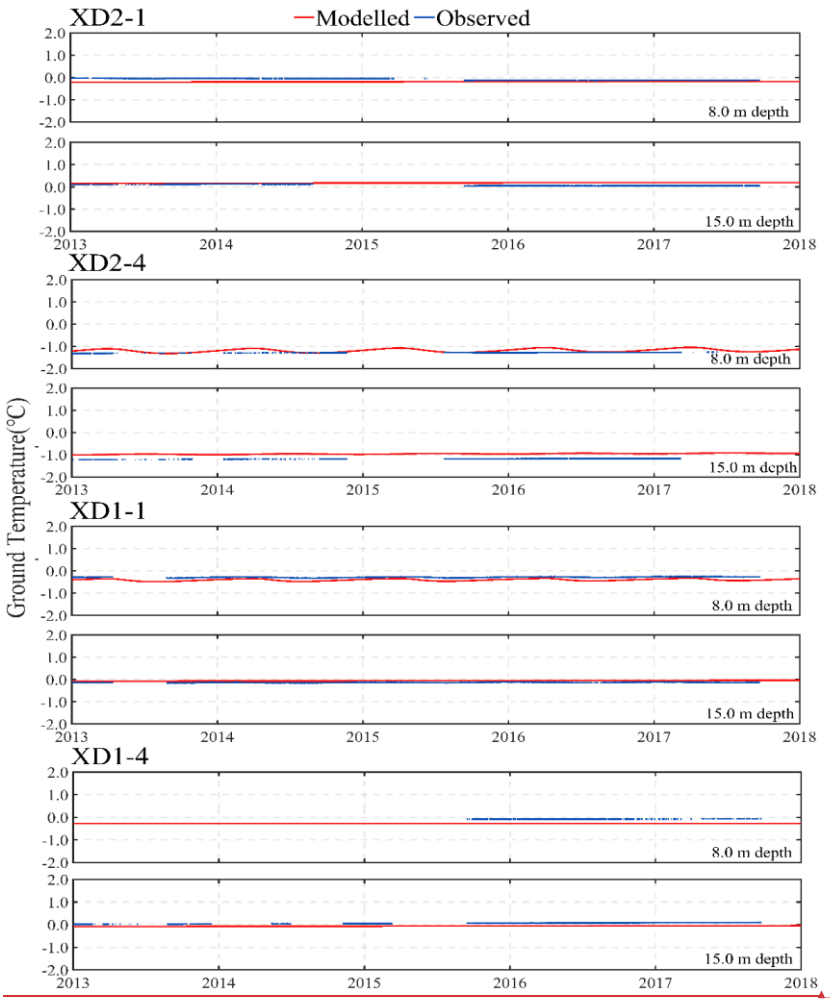

设置了格式: 英语(美国)

Figure A4. Same as Figure 4. but for daily mean ground temperature at 8 m, and 15 m

带格式的: 左, 缩进: 首行缩进: 0 字符, 段落间距段前: 12 磅, 段后: 12 磅

Code and data availability. Monitoring data *in-situ* from the field observation sites provided by the Cryosphere Research Station on Qinghai-Xizang Plateau of the Chinese Academy of Sciences (CAS) is available online https://data.tpdc.ac.cn/en/disallow/789e838e-16ac-4539-bb7e-906217305a1d/ (Zhao et al., 2021), and https://doi.org/10.1007/s11629-017-4731-2, (Luo et al., 2018), respectively. Improved MODIS LST data were provided by (Zou et al., 2017) (https://doi.org/10.5194/tc-11-2527-2017). The historical official observed daily AT series are available from the China

Meteorological Data Sharing Service System (http://data.cma.cn/data/cdcdetail/dataCode/A.0012.0001.html). Climate projections of CMIP5 and CMIP6 data are freely available online at (https://interactive-atlas.ipcc.ch) (Iturbide et al., 2020). The Shuttle Radar Topography Mission (SRTM) with a 1-arcsecond (~30 m) DEM data were from Hole-filled seamless SRTM data V4, International Centre for Tropical Agriculture (CIAT), available at: http://srtm.csi.cgiar.org (Jarvis et al., 2008). Three existing permafrost distribution maps investigated in 1975, 2012, and 2016 were available by Nan et al. (2003) (https://doi.org/10.1007/s11629-017-4731-2), Luo et al. (2018) (https://doi.org/10.1007/s11629-017-4731-2), and Zou et al. (2017) (https://doi.org/10.5194/tc-11-2527-2017). The new permafrost model source code is available on request form the first authors or corresponding authors or co-authors of this study: Jianting Zhao, jt.zhao@nuist.edu.cn; Lin Zhao, lzhao@nuist.edu.cn; Zhe Sun, sunzhe@lzb.ac.cn.

Author contribution. LZ conceived and conceptualized the idea; JZ and ZS developed the methodology; LZ, ZS, and GH supervised the study; JZ, MX, LY, and SW performed data processing and analyses. LZ and FN acquired the funding and provided the resources; FN, DZ, GL, DE, CW, YQ, JS, and HZ participated in the fieldwork and maintained the observation sites; JZ wrote the draft version, and ZS, FN, GH, LW, JG, YW, YL, WY, and ZX reviewed and edited the writing.

Competing interests. The author has declared that neither they nor their co-authors have any conflict of interest.

Acknowledgments. ~~This study was jointly supported by the National Natural Science Foundation of China (grant no. 41931180) and the Second Tibetan~~Tibet ~~Plateau Scientific Expedition and Research (STEP) program (grant no. 2019QZKK0201, 2019QZKK0905). Furthermore, a~~ A warm thanks to all the scientists, engineers, and students who participated in the field measurement and helped to maintain the observation network for data acquisition.

Financial support. This study was jointly supported by the National Natural Science Foundation of China (grant no. 41931180) and the Second Tibet Plateau Scientific Expedition and Research (STEP)

带格式的: 段落间距段前: 12 磅, 段后: 12 磅

带格式的: 段落间距段前: 12 磅, 段后: 12 磅

program (grant no. 2019QZKK0201, 2019QZKK0905).

References

Buteau, S., Fortier, R., Delisle, G., and Allard, M.: Numerical simulation of the impacts of climate warming on a permafrost mound, Permafrost and Periglac. Process., 15, 41-57, https://doi.org/10.1002/ppp.474, 2004.

Bense, V., Kooi, H., Ferguson, G., Read, T.: Permafrost degradation as a control on hydrogeological regime shifts in a warming climate, J Geophys Res Earth Surf 117. https://doi.org/10.1029/2011JF002143, 2012.

Cao, Y., Sheng, Y., Wu, J., Li, J., Ning, Z., Hu, X., Feng, Z., and Wang, S.: Influence of upper boundary conditions on simulated ground temperature field in permafrost regions, J. Glaciol Geocryol., 36, 802-810, doi: 10.7522 / j. issn.1000-0240.2014.0096,2014.

Chang, Y., Lyu, S., Luo, S., Li, Z., Fang, X., Chen, B., Chen, S., Li, R., and Chen, S.: Estimation of permafrost on the Tibetan Plateau under current and future climate conditions using the CMIP5 data, Int. J. Climatol., 38: 5659–5676. https://doi.org/10.1002/joc.5770, 2018.

Cheng, G. and Jin, H.: Permafrost and groundwater on the Qinghai Tibet Plateau and in Northeast China, Hydrogeol. J., 21, 5–23, https://doi.org/10.1007/s10040-012-0927-2, 2013.

Cheng, G. and Wu, T.: Responses of permafrost to climate change and their environmental significance, Qinghai-Tibet Plateau, J. Geophys. Res., 112, 1–10, https://doi.org/10.1029/2006JF000631, 2007.

Cheng, G.: Problems on zonation of high-altitude permafrost, Ac. Geogr. Sin., 39, 185–193, 1984.

Cheng, G.: Influences of local factors on permafrost occurrence and their implications for Qinghai-Xizang Railway design, Sci China Ser D: Earth Sci., 47, 704–709, https://doi.org/10.1007/BF02893300, 2004.

Cheng, G., Zhao, L., Li, R., Wu, X., Sheng, Y., Hu, G., Zou, D., Jin, H., Li, X., and Wu, Q.: Characteristic, changes and impacts of permafrost on Qinghai-Tibet Plateau, Chinese Sci. Bull., 64, 2783–2795, doi: 10.1360/TB-2019-0191, 2019.

Construction Ministry of PRC.: Code for design of soil and foundation of building in frozen soil region, China Architecture and Building Press, Beijing, China, 2011.

Fewster, R., Morris, P., Ivanovic, R., Swindles, G., Peregon, A., and Smith, C.: Imminent loss of climate space for permafrost peatlands in Europe and Western Siberia, Nat. Clim. Chang, 12, 373–379, https://doi.org/10.1038/s41558-022-01296-7, 2022.

Guo, D., and Wang, H.: CMIP5 permafrost degradation projection: a comparison among different

带格式的: 缩进: 左侧: 0 厘米, 悬挂缩进: 1.5 字符, 首行缩进: -1.5 字符

设置了格式: 字体颜色: 文字 1

regions. J. Geophys. Res. Atmos.,121, 4499–4517, https://doi.org/10.1002/2015JD024108, 2016.

Guo, D., Wang, H., and Li, D. 2012. A projection of permafrost degradation on the Tibetan Plateau during the 21st century. 117, D05106. Journal of Geophysical Research: Atmospheres. https://doi.org/10.1029/2011JD016545.

Hanna Lee, H., Swenson, S., Slater, A., and Lawrence, D.: Effects of excess ground ice on projections of permafrost in a warming climate, Environ. Res. Lett. 9 124006, doi:10.1088/1748-9326/9/12/124006, 2014.

Hipp, T., Etzelmüller, B., Farbrot, H., Schuler, T., and Westermann, S.: Modelling borehole temperatures in Southern Norway–insights into permafrost dynamics during the 20th and 21st century, The Cryosphere, 6, 553–571, https://doi.org/10.5194/tc-6-553-2012, 2012.

Hjort, J., Streletskiy, D., Doré, G., Wu, Q., Bjella, K., and Luoto, M.: Impacts of permafrost degradation on infrastructure, Nat. Rev. Earth Environ., 3, 24-38, https://doi.org/10.1038/s43017-021-00247-8, 2022.

Hu, G., Zhao, L., Wu, X., Li, R., Wu, T., Xie, C., Pang, Q., and Zou, D.: Comparison of the thermal conductivity parameterizations for a freeze-thaw algorithm with a multi-layered soil in permafrost regions, Catena, 156, 244-251, http://dx.doi.org/10.1016/j.catena.2017.04.011, 2017.

IPCC. Climate change 2021: the physical science basis, https://www.ipcc.ch/report/ar6/wg1/downloads/report/IPCC_AR6_WGI_Full_Report.pdf., 2021.

IPCC.: Special report on the ocean and cryosphere in a changing climate, https://archive.ipcc.ch/srocc/, 2019.

Iturbide, M., Gutiérrez, J., Alves, L., Bedia, J., Cerezo-Mota, R., Cimadevilla, E., Cofiño, A., Di, L., Faria, S., Gorodetskaya, I., Hauser, M., Herrera, S., Hennessy, K., Hewitt, H., Jones, R., Krakovska, S., Manzanas, R., Martínez-Castro, D., Narisma, G., Nurhati, I., Pinto, I., Seneviratne, S., van den Hurk, B., and Vera, C.: An update of IPCC climate reference regions for subcontinental analysis of climate model data: definition and aggregated datasets, Earth Syst. Sci. Data, 12, 2959–2970, https://doi.org/10.5194/essd-12-2959-2020,2020.

Jafarov, E., Marchenko, S., and Romanovsky, V.: Numerical modeling of permafrost dynamics in Alaska using a high spatial resolution dataset., The Cryosphere, 6, 613-624, https://tc.copernicus.org/articles/6/613/2012/, 2012.

Jarvis, A., Reuter, H., Nelson, A., and Edith, G.: Hole-filled seamless SRTM data V4, Tech. rep., International Centre for Tropical Agriculture (CIAT), Cali, Columbia, available at: http://srtm.csi.cgiar.org, 2008.

设置了格式: 字体颜色: 自定义颜色(RGB(34,34,34)), 英语(美国), 图案: 清除 (白色)

带格式的: 缩进: 左侧: 0 厘米, 悬挂缩进: 1.5 字符, 首行缩进: -1.5 字符

Jin, H., Li, S., Cheng, G., Wang, S., and Li, X.: Permafrost and climatic change in China, Global Planet. Change., 26, 387-404, https://doi.org/10.1016/S0921-8181(00)00051-5, 2000.

Jin, H., Luo, D., Wang, S., Lü, L., and Wu, J.: Spatiotemporal variability of permafrost degradation on the Qinghai-Tibet Plateau, Sci. Cold Arid Reg., 3, 281–305, DOI: 10.3724/SP.J.1226.2011.00281, 2011.

Jin, H., Wu, Q., and Romanovsky, V.: Degrading permafrost and its impacts, Adv. Clim. Change Res.,12, https://doi.org/10.1016/ j. accre.2021.01.007,2021.

Jin, H., Zhao, L., Wang, S., and Jin, R.: Thermal regimes and degradation modes of permafrost along the Qinghai-Tibet Highway, Sci. China Ser. D: Earth Sci., 49, 1170–1183, https://doi.org/10.1007/s11430-006-2003-z, 2006.

~~Kane, D., Hinkel, K., Goering, D., Hinzman, L., Outcalt, S.: Non-conductive heat transfer associated with frozen soils, Global Planet. Change., 29, 275-292, https://doi.org/10.1016/S0921-8181(01)00095-9,2001.~~

Lawrence, D., Slater, A., and Swenson, S: Simulation of Present-Day and Future Permafrost and Seasonally Frozen Ground Conditions in CCSM4, J. Clim., 25, 2207-2225, https://doi.org/10.1175/JCLI-D-11-00334.1, 2012.

Li, D., Chen, J., Meng, Q., Liu, D., Fang, J., and Liu, J.: Numeric simulation of permafrost degradation in the eastern Tibetan Plateau, Permafrost and Periglac. Process., 19, 93-99, https://doi.org/10.1002/ppp.611,2008.

Li, R., Zhao, L., Ding, Y., Wu, T., Xiao, Y., Du, E., Liu, G., and Qiao, Y.: Temporal and spatial variations of the active layer along the Qinghai-Tibet Highway in a permafrost region, Chinese Sci. Bull., 57, 4609–4616, https://doi.org/10.1007/s11434-012-5323- 8, 2012

Li, S., Cheng, G., and Guo, D.: The future thermal regime of numerical simulating permafrost on the Qinghai-Xizang (Tibet) Plateau, China, under a warming climate. Science in China, Ser. D, 434-441,1996.

Li, W., Zhao, L., Wu, X., Zhao, Y., Fang, H., and Shi, W.: Distribution of soils and landform relationships in the permafrost regions of Qinghai-Xizang (Tibetan) Plateau, Chinese Sci. Bull., 60, 2216–2226, https://doi.org/10.1360/N972014-01206, 2015b.

Li, X., Cheng, G., Jin, H., Kang, E., Che, T., Jin, R., Wu, L., Nan, Z., Wang, J., and Shen, Y.: Cryospheric Change in China, Global Planet. Change., 62, 210–218, https://doi.org/10.1016/j.gloplacha.2008.02.001, 2008.

Liu, G., Xie, C., Zhao, L., Xiao, Y., Wu, T., Wang, W., and Liu, W.: Permafrost warming near the northern limit of permafrost on the Qinghai–Tibetan Plateau during the period from 2005 to 2017, A case study in the Xidatan area, Permafrost and Periglac. Process., 32: 323– 334, https://doi.org/10.1002/ppp.2089, 2020.

Lu, Q., Zhao, D. and Wu, S.: Simulated responses of permafrost distribution to climate change on the Qinghai–Tibet Plateau. Sci. Rep., 7, 3845. https://doi.org/10.1038/s41598-017-04140-7, 2017.

Luo, J., Niu, F., Lin, Z., Liu, M., and Yin, G.: Variations in the northern permafrost boundary over the last four decades in the Xidatan region, Qinghai–Tibet Plateau. J. Mt. Sci., 15, 765–778, https://doi.org/10.1007/s11629-017-4731-2, 2018.

Miner, K., Turetsky, M., Malina, E., Bartsch, A., Tamminen, J., McGuire, A., Fix, A., Sweeney, C., Elder, C., and Miller, C.: Permafrost carbon emissions in a changing Arctic, Nat. Rev. Earth Environ, 3, 55–67, https://doi.org/10.1038/s43017-021-00230-3, 2022.

Nan, Z., Gao, Z., Li, S., and Wu, T.: Permafrost changes in the northern limit of permafrost on the Qinghai-Tibet plateau in the last 30 years, J. Geogr. Sci., 58, 817-823, 2003.

Ni, J., Wu, T., Zhu, X., Hu, G., Zou, D., Wu, X., Li, R., Xie, C., Qiao, Y., Pang, Q., Hao, J., and Yang, C.: Simulation of the present and future projection of permafrost on the Qinghai-Tibet Plateau with statistical and machine learning models, J. Geophys. Res. Atmos.,126, e2020JD033402, https://doi.org/10.1029/2020JD033402, 2021.

Nitze, I., Grosse, G., Jones, B. M., Romanovsky, V. E., and Boike, J.: Remote sensing quantifies widespread abundance of permafrost region disturbances across the Arctic and Subarctic, Nat. Commun., 9, 5423, https://doi.org/10.1038/s41467-018-07663-3,2018.

Obu, J., Westermann, S., Bartsch, A., Berdnikov, N., Christiansen, H., Dashtseren, A., Delaloye, R., Elberling, B., Etzelmüller, B., Kholodov, A., Khomutov, A., Kääb, A., Leibmanc, M., Lewkowicz, A., Panda, S., Romanovsky, V., Way, R., Westergaard-Nielsen, A., Wu, T., Yamkhin, J., and Zou, D.: Northern Hemisphere permafrost map based on TTOP modelling for 2000–2016 at 1 km2 scale, Earth-Sci. Rev., 193, 299-316, https://doi.org/10.1016/j.earscirev.2019.04.023, 2019.

Qin, D. Glossary of cryosphere science. Meteorological Press, Beijing, China, 2014.

Ran, Y., Li, X., Cheng, G., Zhang, T., Wu, Q., Jin, H., and Jin, R.: Distribution of permafrost in China: an overview of existing permafrost maps, Permafrost and Periglac. Process., 23: 322-333. https://doi.org/10.1002/ppp.1756, 2012.

Riseborough, D., Shiklomanov, N., Etzelmüller B, Gruber, S., and Marchenko, S.: Recent advances in permafrost modelling, Permafrost and Periglac. Process., 19, 137–156, https://doi.org/10.1002/ppp.615, 2008.

Schädel, C., Bader, M., Schuur, E., Biasi, C., Bracho, R., Čapek, P., Baets, S., Baets, S., Diáková, K., Ernakovich, J., Aragones, C., Graham, D., Hartley, I., Iversen, C., Kane, E., Knoblauch, C., Lupascu, M., Martikainen, P., Natali, S., Norby, R., O'Donnell, J., Chowdhury,T., Šantrůčková, H., Shaver, G., Sloan, V., Treat, C., Turetsky, M., Waldrop, M., and Wickland, K.: Potential carbon emissions dominated by carbon dioxide from thawed permafrost soils, Nature Clim. Change, 6, 950–953, https://doi.org/10.1038/nclimate3054, 2016.

Schiesser, W.: The Numerical Method of Lines: Integration of Partial Differential Equations, vol. 212, Academic Press, San Diego, USA, 1991.

Smith, S., O'Neill, H., Isaksen, K., Noetzli, J., and Romanovsky, V.: The changing thermal state of permafrost, Nat. Rev. Earth Environ., 3, 10–23https://doi.org/10.1038/s43017-021-00240-1, 2022.

Sun, Z., Zhao, L., Hu, G., Qiao, Y., Du, E., Zou, D., Xie, C.: Modeling permafrost changes on the Qinghai-Tibetan plateau from 1966 to 2100: a case study from two boreholes along the Qinghai-Tibet engineering corridor. Permafrost and Periglac. Process., 32:156-171, https://doi.org/10.1002/ppp.2022, 2019.

Sun, Z., Zhao, L., Hu, G., Zhou, H., Liu, S., Qiao, Y., Du, E., Zou, D., and Xie, C.: Numerical simulation of thaw settlement and permafrost changes at three sites along the Qinghai-Tibet Engineering Corridor in a warming climate, Geophysical Research Letters, 49, e2021GL097334, https://doi.org/10.1029/2021GL097334, 2022.

Sjöberg, Y., Coon, E., Sannel, A., Pannetier, R., Harp, D., Frampton, A., Painter, S., Lyon SW.: Thermal effects of groundwater flow through subarctic fens: a case study based on field observations and numerical modeling, Water Resour Res 52:1591–1606.https://doi.org/10.1002/2015WR017571, 2016.

Wang, C., Wang, Z., Kong, Y. Zhang, F., Yang, K., and Zhang, T.: Most of the Northern Hemisphere Permafrost Remains under Climate Change, Sci. Rep., 9, 3295, https://doi.org/10.1038/s41598-019-39942-4, 2019.

Wang, S., Jin, H., Li, S., and Zhao, L.: Permafrost degradation on the Qinghai-Xizang (Tibet) Plateau and its environmental impacts, Permafrost and Periglac. Process.,11: 43-53, https://doi.org/10.1002/(SICI)1099-1530(200001/03)11:1<43: AID-PPP332>3.0.CO;2-H, 2000.

Westermann, S., Langer, M., Boike, J., Heikenfeld, M., Peter, M., Etzelmüller, B., and Krinner, G.: Simulating the thermal regime and thaw processes of ice-rich permafrost ground with the land-surface model CryoGrid3, Geosci. Model Dev., 9, 523–546, https://doi.org/10.5194/gmd-9-523-2016, 2016.

Westermann, S., Schuler, T. V., Gisnås, K., and Etzelmüller, B.:Transient thermal modeling of permafrost conditions in Southern Norway, The Cryosphere, 7, 719-739, https://tc.copernicus.org/articles/7/719/2013/, 2013.

~~Weismüller, J., Wollschläger, U., Boike, J., Pan, X., Yu, Q., and Roth, K.: Modeling the thermal dynamics of the active layer at two contrasting permafrost sites on Svalbard and on the Tibetan Plateau, The Cryosphere, 5, 741–757, doi:10.5194/tc-5741-2011, 2011.~~

Westermann, S., Langer, M., Boike, J., Heikenfeld, M., Peter, M., Etzelmüller, B., and Krinner, G.: Simulating the thermal regime and thaw processes of ice-rich permafrost ground with the land-surface model CryoGrid 3, Geosci. Model Dev., 9, 523–546, https://doi.org/10.5194/gmd-9-

带格式的: 缩进: 左侧: 0 厘米, 悬挂缩进: 1.5 字符, 首行缩进: -1.5 字符

设置了格式: 字体颜色: 文字 1

设置了格式: 非突出显示

设置了格式: 非突出显示

523-2016, 2016

Willmott, C., and Matsuura, K.: Advantages of the mean absolute error (MAE) over the root mean square error (RMSE) in assessing average model performance, Clim. Res., 30, 79–82, doi:10.3354/cr030079, 2005.

Wu, J., Sheng, Y., Wu, Q., and Wen, Z.: Processes and modes of permafrost degradation on the Qinghai-Tibet Plateau, Sci. China Ser. D: Earth Sci., 53, 150–158, https://doi.org/10.1007/s11430-009-0198-5, 2010.

Wu, Q. and Zhang, T.: Recent permafrost warming on the Qinghai-Tibetan Plateau, J. Geophys. Res., 113, D13108, doi:10.1029/2007JD009539, 2008.

Wu, Q., Zhang, T., and Liu, Y.: Permafrost temperatures and thickness on the Qinghai-Tibet Plateau, Global Planet. Change., 72, 32-38, https://doi.org/10.1016/j.gloplacha.2010.03.001, 2010.

Wu, T., Li, S., Cheng, G., and Nan, Z.: Using ground-penetrating radar to detect permafrost degradation in the northern limit of permafrost on the Tibetan plateau, Cold Reg. Sci. Technol., 41,211-219, https://doi.org/10.1016/j.coldregions.2004.10.006, 2005.

Wu, X., Nan, Z., Zhao, S., Zhao, L., and Cheng, G.: Spatial modeling of permafrost distribution and properties on the Qinghai-Tibet Plateau, Permafrost and Periglac. Process., 29, 86-99, https://doi.org/10.1002/ppp.1971, 2018.

Xiao, Y., Zhao, L., Dai, Y., Li, R., Pang, Q., and Yao, J.: Representing permafrost properties in CoLM for the Qinghai–Xizang (Tibetan) plateau, Cold Reg. Sci. Technol., 87, 68-77, http://dx.doi.org/10.1016/j.coldregions.2012.12.004, 2013.

Xu, Y., Shen, Y., and Wu, Z.: Spatial and Temporal Variations of Land Surface Temperature Over the Tibetan Plateau Based on Harmonic Analysis, Mt. Res. Dev., 33, 85–94, https://doi.org/10.1659/MRD-JOURNAL-D-12-00090.1,2013.

Yang, M., Nelson, F. E., Shiklomanov, N. I., Guo, D., and Wan, G.: Permafrost degradation and its environmental effects on the Tibetan Plateau: A review of recent research, Earth-Sci. Rev., 103, 31–44, 2010.

Yao, T., Xue, Y., Chen, D., Chen, F., Thompson, L., Cui, P., Koike, T., Lau, W. K., Lettenmaier, D., Mosbrugger, V., Zhang, R., Xu, B., Dozier, J., Gillespie, T., Gu, Y., Kang, S., Piao, S., Sugimoto, S., Ueno, K., Wang, L., Wang, W., Zhang, F., Sheng, Y., Guo, W., , Yang, X., Ma, Y., Shen, S. S. P., Su, Z., Chen, F., Liang, S., Liu, Y., Singh, V. P., Yang, K., Yang, D., Zhao, X., Qian, Y., Zhang, Y., and Li, Q.: Recent Third Pole's Rapid Warming Accompanies Cryospheric Melt and Water Cycle Intensification and Interactions between Monsoon and Environment: Multidisciplinary Approach with Observations, Modeling, and Analysis, B. Am. Meteorol. Soc., 100, 423-444, https://doi.org/10.1175/BAMS-D-17-0057.1, 2019.

Yershov, E.: Principles of Geocryology, Lanzhou University Press, Lanzhou, China, 2016.

设置了格式: 非突出显示

设置了格式: 非突出显示

Yi, S., Wang, X., Qin, Y., Xiang, B., and Ding, Y.: Responses of alpine grassland on Qinghai–Tibetan plateau to climate warming and permafrost degradation: a modeling perspective, Environ. Res. Lett., 9,074014, https://doi.org/10.1088/1748-9326/9/7/074014,2014.

Yin, G., Luo, J., Niu, F., Lin, Z., and Liu, M.: Thermal regime and variations in the island permafrost near the northern permafrost boundary in Xidatan, Qinghai–Tibet Plateau, Front. Earth Sci., 560, https://doi.org/10.3389/feart.2021.708630, 2021.

Yin, G., Niu, F., Lin, Z., Luo, J., and Liu, M.: Data-driven spatiotemporal projections of shallow permafrost based on CMIP6 across the Qinghai–Tibet Plateau at 1 km2 scale, Adv. Clim. Change Res., 12, 814-827, https://doi.org/10.1016/j.accre.2021.08.009, 2021.

Yue, G., Zhao, L., Zhao, Y., Du, E., Wang, Q., Wang, Z., and Qiao, Y.: Relationship between soil properties in permafrost active layer and surface vegetation in Xidatan on the Qinghai-Tibetan Plateau, J. Geogr. Sci., 35, 565-573, doi: 10.7522/j. issn. 1000-0240.2013.0065, 2013.

~~Zhang, G., Nan, Z., Zhao, L., Liang, Y., and Cheng, G.: Qinghai-Tibet Plateau wetting reduces permafrost thermal responses to climate warming, Earth and Planetary Sc. Lett., 562, 116858, https://doi.org/10.1016/j.epsl.2021.116858, 2011.~~

Zhang, G., Nan, Z., Hu, N., et al. 2022. Qinghai-Tibet Plateau permafrost at risk in the late 21st Century. Earth's Future. 10, e2022EF002652. https://doi.org/10.1029/2022EF002652.

Zhang, Y., Wang, X., Fraser, R., Olthof, I., Chen, W., Mclennan, D., Ponomarenko, and S.,Wu, W.: Modelling and mapping climate change impacts on permafrost at high spatial resolution for an Arctic region with complex terrain, The Cryosphere, 7, 1121–1137, https://doi.org/10.5194/tc-7-1121-2013, 2013.

Zhao L, Ding Y, Liu G, Wang S, and Jin H.: Estimates of the reserves of ground ice in permafrost regions on the Tibetan plateau, J. Glaciol Geocryol., 32:1-9, 2010.

Zhao, L. and Sheng, Y.: Permafrost survey manual, Science Press, Beijing, 13–14, 2015.

Zhao, L., Hu, G., Zou, D., Wu, X., Ma, L., Sun, Z., Yuan, L., Zhou, H., and Liu, S.: Permafrost Changes and Its Effects on Hydrological Processes on Qinghai-Tibet Plateau, Bull. Chin. Acad. Sci., 34, 1233–1246, DOI: 10.16418/j.issn.1000-3045.2019.11.006, 2019.

Zhao, L., Wu, Q., Marchenko, S. S., and Sharkhuu, N.: Thermal state of permafrost and active layer in Central Asia during the international polar year, Permafrost and Periglac. Process., 21, 198–207, https://doi.org/10.1002/ppp.688, 2010.

Zhao, L., Zou, D. Hu, G., Du, E., Pang, Q., Xiao, Y., Li, R., Sheng, Y., Wu, X., Sun, Z., Wang, L., Wang, C., Ma, L., Zhou, H., and Liu, S.: Changing climate and the permafrost environment on the Qinghai–Tibet (Xizang) Plateau, Permafrost Periglac., 31, 396–405, https://doi.org/10.1002/ppp.2056, 2020.

Zhao, L., Zou, D., Hu, G., Wu, T., Du, E., Liu, G., Xiao, Y., Li, R., Pang, Q., Qiao, Y., Wu, X., Sun, Z., Xing, Z., Sheng, Y., Zhao, Y., Shi, J., Xie, C., Wang, L., Wang, C., and Cheng, G.: A synthesis dataset of permafrost thermal state for the Qinghai–Tibet (Xizang) Plateau, China, Earth Syst. Sci. Data, 13, 4207–4218, https://doi.org/10.5194/essd-13-4207-2021, 2021.

Zhou, Y., Guo, D., Qiu, G., Cheng, G., and Li, S.: China Permafrost, Science Press, Beijing, 145–151, 2000.

Zou, D., Zhao, L., Sheng, Y., Chen, J., Hu, G., Wu, T., Wu, J., Xie, C., Wu, X., Pang, Q., Wang, W., Du, E., Li, W., Liu, G., Li, J., Qin, Y., Qiao, Y., Wang, Z., Shi, J., and Cheng, G.: A new map of permafrost distribution on the TibetanTibet Plateau, The Cryosphere, 11, 2527–2542, https://doi.org/10.5194/tc-11-2527-2017, 2017.

Zou, D., Zhao, L., Wu, T., Wu, X., Pang, Q., and Wang, Z.: Modeling ground surface temperature by means of remote sensing data in high-altitude areas: test in the central Tibetan Plateau with application of moderate-resolution imaging spectroradiometer Terra/Aqua land surface temperature and ground based infrared radiometer, J. Appl. Remote Sens., 8, 083516, https://doi.org/10.1117/1.JRS.8.083516, 2014.